Scalable Fast Dispersive Scanner

A thesis submitted to the
Graduate School of Natural and Applied Sciences

by

Rasül TORUN

in partial fulfillment for the
degree of Master of Science

in
Electronics and Computer Engineering

This is to certify that we have read this thesis and that in our opinion it is fully adequate, in scope and quality, as a thesis for the degree of Master of Science in Electronics and Computer Engineering.

APPROVED BY:

Assoc. Prof. Özdal Boyraz .....
(Thesis Advisor)

Assist. Prof. Kemal Özdemir .....

Prof. Dr. Muammer Koç .....

This is to confirm that this thesis complies with all the standards set by the Graduate School of Natural and Applied Sciences of İstanbul Şehir University:

DATE OF APPROVAL: 17 July 2014

SEAL/SIGNATURE:

Declaration of Authorship

I, Rasül TORUN, declare that this thesis titled, 'Scalable Fast Dispersive Scanner' and the work presented in it are my own. I confirm that:

- This work was done wholly or mainly while in candidature for a research degree at this University.
- Where any part of this thesis has previously been submitted for a degree or any other qualification at this University or any other institution, this has been clearly stated.
- Where I have consulted the published work of others, this is always clearly attributed.
- Where I have quoted from the work of others, the source is always given. With the exception of such quotations, this thesis is entirely my own work.
- I have acknowledged all main sources of help.
- Where the thesis is based on work done by myself jointly with others, I have made clear exactly what was done by others and what I have contributed myself.

Signed: 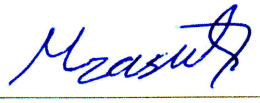

Date: 17.07.2014

Scalable Fast Dispersive Scanner

Rasül Torun

Abstract

Rapid progress in CMOS technology with the availability of parallel computing increased the frequency of operation in digital signal processing. However, ADCs could not suffice high speeds more than a few GSa/s. At this point, an optical time-stretching technique is facilitated to increase the ADC effective sampling rates with slowing down the RF signals. Later, the technique is employed in Optical Arbitrary Waveform Generation and Optical Real-time Imaging.

This thesis is devoted to the investigation of such Photonic Time Stretch technique and its applications such as Time Stretch ADC and Real-time Imaging. The Time-Stretch ADC system is examined both experimentally and with simulations. On the other hand, a novel fast dispersive laser scanning system is demonstrated by using MEMS based digital micro-mirror arrays technology. The proposed technique employs real-time dispersive imaging system, which captures spectrally encoded images with a single photodetector at pulse repetition rate via space-to-time mapping technology. Wide area scanning capability is introduced by using individually addressable micro mirror arrays as a beam steering device.

Experimentally, we scanned $\sim$20mm^2 at scan rate of 5kHz with $\sim$150μm lateral and $\sim$160μm vertical resolution that can be controlled by using 1024x768 mirror arrays. With the current state of art MEMS technology, fast scanning with $<$30μs and resolution down to single mirror pitch size of 10.8μm is also achievable.

Keywords: Amplified Dispersive Fourier Transform, Time-Stretch Analog to Digital Converter, Real Time Imaging, Surface Metrology, Quality Control

Ölçeklenebilir Hızlı Dispersiv Tarayıcı

Rasül Torun

Öz

CMOS teknolojisindeki hızlı ilerleme paralel hesaplama sistemleriyle birleşince dijital sinyal işleme hızları yükseldi. Fakat A/D çeviriciler saniyede birkaç milyar örneklemeden öteye gidemediler. Bu noktada, Optik tabanlı Zaman Esnemesi tekniği kullanılmış ve optik bir atıma bindirilen Radyo Frekans sinyali yavaşlatılarak, A/D çeviricilerin efektif örnekleme hızı arttırılmıştır. Daha sonra bu teknik, Optik tabanlı Rasgele Dalga Formu Jeneratörü ve Gerçek Zamanlı Optik Görüntüleme uygulamalarında da kullanılmıştır.

Bu tez, bu Fotonik Zaman Esnemesi tekniğinin ve bu tekniğin A/D çeviriciler ve optik görüntüleme alanlarındaki uygulamaları üzerine yapılmıştır. Bu çalışmada, Zaman Esnemeli A/D Çeviriciler deneysel olarak ve simülasyonları yapılarak incelenmiştir. Diğer taraftan, MEMS tabanlı dijital mikro ayna teknolojisi kullanılarak yeni bir hızlı dispersiv lazer tarama sistemi kurulmuştur. Bu çalışmada sunulan teknik, gerçek zamanlı dispersiv görüntüleme sistemi kullanmaktadır. Bu sistem, tek bir fotodedektörle spektral olarak kodlanmış görüntüyü uzay-zaman eşleştirme teknolojisi kullanarak atım frekansında yakalamaktadır. Sistemin geniş alan tarama kabiliyeti, tek tek kontrol edilebilen mikro ayna dizilerini hüzme yönlendirici olarak kullanmamızdan gelmektedir.

Bu sistemle, 1024x768'lik mikro ayna dizilerini kontrol ederek $\sim$20mm^2'lik bir alanı deneysel olarak 5kHz hızla taradık. Bu taramada yatay yönde $\sim$150μm ve dikey yönde $\sim$160μm çözünürlük elde ettik. Günümüzde mevcut olan en iyi dijital mikro ayna sistemleri kullanılarak bu sistem, 30μs'den az bir sürede tarama yaparak tek bir mikro aynanın boyutu olan 10.8μm çözünürlüğe ulaşabilir.

Anahtar Sözcükler: Yükseltilmiş Dağılma Fourier Dönüşümü, Zaman Esnemeli Analogdan Dijitale Çevirici, Gerçek Zamanlı Görüntüleme, Yüzey Ölçümü, Kalite Kontrol

To my family ...

Acknowledgments

I would like to express my sincere gratitude to my advisor, Prof. Özdal Boyraz, for his guidance, support and time. Also, I would like to thank my committee members, Prof. Kemal Özdemir and Prof. Muammer Koç for their time and suggestions.

Additionally, I would like to thank Salih Kalyoncu who helped me to improve my experimental skills and familiarize the field of optics. His advice and supervision was priceless to pursue research in this field.

I gratefully acknowledge the research fellowship received from the Scientific and Technological Research Council of Turkey (TÜBİTAK) during my studies to obtain the Master of Science degree.

In addition, I would like to thank my friend İbrahim Arı, for his valuable ideas and motivating talks. Also, I appreciate the help of Emin Torun for proofreading and editing while preparing the final version of this thesis.

To sum up, special thanks to my family for supporting and encouraging me all the time.

Contents

List of Figures

List of Tables

Abbreviations

ADC	**A**nalog-to-**D**igital **C**onverter
AOD	**A**cousto-**o**ptic **D**eflector
AWG	**A**rbitrary **W**aveform **G**eneration
CCD	**C**harge **C**oupled **D**evice
CFBG	**C**hirped **F**iber **B**ragg **G**rating
CMOS	**C**omplementary **M**etal **O**xide **S**emiconductor
CW	**C**ontinuous **W**ave
CWDM	**C**oarse **W**avelength **D**ivision **M**ultiplexing
DCM	**D**ispersion **C**ompensation **M**odule
DFT	**D**ispersive **F**ourier **T**ransform
DMD	**D**igital **M**icro mirror **D**evice
DSP	**D**igital **S**ignal **P**rocessor
EDFA	**E**rbium **D**oped **F**iber **A**mplifier
EOM	**E**lectro-**o**ptic **M**odulator
FOV	**F**ield **o**f **V**iew
GSa	**G**iga **S**ample
GVD	**G**roup **V**elocity **D**ispersion
LC	**L**iquid **C**rystal
LCD	**L**iquid **C**rystal **D**isplay
LIDAR	**Li**ght **D**etection **a**nd **R**anging
MEMS	**M**icro**e**lectro**m**echanical **S**ystems
MLL	**M**ode **L**ocked **L**aser
MZ	**M**ach **Z**ehnder
MZI	**M**ach **Z**ehnder **I**nterferometer
NLSE	**N**on**l**inear **S**chrödinger **E**quation

NIR	**N**ear **I**nfra-**R**ed
PWM	**P**ulse **W**idth **M**odulation
SC	**S**uper**c**ontinuum
SLM	**S**patial **L**ight **M**odulator
SMF	**S**ingle **M**ode **F**iber
SNR	**S**ignal to **N**oise **R**atio
SPM	**S**elf **P**hase **M**odulation
SRAM	**S**tatic **R**andom **A**ccess **M**emory
SRS	**S**timulated **R**aman **S**cattering
SSFM	**S**plit **S**tep **F**ourier **M**ethod
THz	**T**era **H**ertz
TS-ADC	**T**ime **S**tretch **A**nalog-to-**D**igital **C**onverter
USAF	**U**nited **S**tates **A**ir **F**orce
UV	**U**ltra-**V**iolet
WIB	**W**avelength **I**nsensitive **B**iasing
XPM	**C**ross **P**hase **M**odulation
YIG	**Y**ttrium **i**ron **g**arnet

Physical Constants

Speed of Light	c	$=$	$2.997\ 924\ 58 \times 10^{8}$ m/s (exact)
Vacuum Permittivity	ε_0	$=$	$8.854\ 187\ 817 \times 10^{-12}$ F/m
Vacuum Permeability	μ_0	$=$	$4\pi \times 10^{-7}$ H/m

Symbols

Symbol	Name	Unit
E	electric field vector	V/m
H	magnetic field vector	A/m
D	electric flux density	C/m^2
B	magnetic flux density	Wb/m^2
P	induced electric polarization vector	C/m^2
M	induced magnetic polarization vector	Wb/m^2
n	refractive index	unitless
L	propagation length	m
L_{eff}	effective length	m
L_D	disperion length	m
L_{NL}	nonlinear length	m
L_A	amplification period	m
ϕ_{NL}	nonlinear phase	radian
z	distance	m
t	time	s
z_0	soliton period	m
N	soliton order	unitless
P_0	peak power	Watt
T_0	pulse width	s
f	frequency	Hz
ω	angular frequency	rad/s
ω_0	central frequency	Hz
$\Delta\omega$	bandwidth	Hz

α	absorption coefficient	m^{-1}
ε_r	relative permittivity	unitless
β_0	wave number	rad/m
λ	wavelength	nm
υ_p	phase velocity	m/s
Ω	frequency shift	rad/s

Chapter 1

Introduction

The idea of time stretching, as a technique to slow down electrical signals, goes back to the mid 19^{th} century. It facilitates linear dispersive elements to manipulate the signal frequency. A novel all-electrical time-stretch system was first demonstrated by William Caputi [1]. The capability of the all-electrical system was limited, since the available dispersive elements in the electrical domain has small bandwidth. On the other hand, ultra-high bandwidth (up to THz) dispersive elements such as single mode fiber (SMF) [2], chirped fiber Bragg gratings (CFBG) [3], and prisms [4], are available in optical domain. Optical time stretch systems that utilize SMF as a dispersive medium, was demonstrated experimentally at the end of the century [5, 6].

The first application employing the technique was the Time Stretch Analog-to-Digital Converter (TS-ADC), since ADC is the key bottleneck in high performance communication systems due to rapid developments in digital signal processor (DSP) technology [7]. Thus, it is necessary to slow down the high frequency electrical signals operated by the DSPs prior to digitization, which could not exceed a few GSa/s sampling rates.

Additionally, time stretching is employed to utilize real-time applications such as optical arbitrary waveform generation (AWG) [2] and optical imaging [8] via slowing down the pulse envelope that is spatially modulated. In such systems, the broadband super continuum (SC) source is followed by the dispersive components, where the broadening effect maps the time and wavelength components, namely time-wavelength mapping. The technique is also called Dispersive Fourier Transform (DFT) [9], since the time domain signal takes the shape of its spectrum at the end of dispersion compensation module (DCM).

This thesis is aimed to explain the DFT and its applications, mainly focused on optical imaging. Chapter 1 is a general introduction to the thesis. In Chapter 2, background information that includes pulse propagation inside the dispersive fiber, optical solitons, Stimulated Raman Scattering (SRS) and optical amplification are delivered. Also, the simulation results obtained by Split Step Fourier Method (SSFM) on group velocity dispersion (GVD), self phase modulation (SPM), and soliton propagation are presented in this chapter. Chapter 3 mentions the general idea of the DFT and provides some simulation and experimental results related to its application as TS-ADC. These two chapters lay the foundation by visiting earlier concepts to make reader familiar with topic. However, in Chapter 4, we proposed a novel wide-field real time imaging technique utilizing MEMS based digital micro mirror devices (DMDs) to observe surface characteristics in microfabrication, microfluidic flow for blood screening in medicine, etc. Experimentally, we scanned $\sim$20 mm^2 wide area at a scan rate of 5 kHz with achieving $\sim$150μm lateral and $\sim$160μm vertical resolution via controlling 1024x768 mirror arrays. With the current state of art equipments, our system can reach fast scanning with less than 30μs and resolution down to single mirror pitch size of 10.8μm [8]. On the other hand, the proposed system can be scaled up in terms of speed, power and area. The speed and power scaling can be achieved via altering DMD and diffraction grating respectively with state of the art equivalents. Additionally, the scanned area can be increased with employing several DMDs in a parallel setup.

Chapter 2

Background Information

2.1 Pulse Propagation in Fibers

2.1.1 Nonlinear Schrödinger Equation

Both linear dispersive and nonlinear effects influence the propagating optical pulses inside a fiber. The linearity in optics is defined by intensity independence [10]; therefore fiber becomes nonlinear especially for intense short pulses ranging from ~10ns to 10fs. Both nonlinear and the dispersive effects change the pulse shape and spectra. As it is well known, light is also an electromagnetic wave; therefore its propagation inside the fiber is governed by Maxwell's equations [11].

$$\nabla \times E = -\frac{\partial B}{\partial t} \tag{2.1a}$$

$$\nabla \times H = J + \frac{\partial D}{\partial t} \tag{2.1b}$$

$$\nabla \cdot D = \rho_f \tag{2.1c}$$

$$\nabla \cdot B = 0 \tag{2.1d}$$

where D (C/m^2) and B (Wb/m^2) are the electric and the magnetic flux densities that are related to corresponding electric and magnetic field vectors E (V/m) and H (A/m)

through equations:

$$D = \varepsilon_0 E + P \tag{2.2a}$$

$$B = \mu_0 H + M \tag{2.2b}$$

where ε_0 (F/m) is the electric permittivity and μ_0 (H/m) is the vacuum permeability which are related to speed of light via the equation c=$\frac{1}{\sqrt{\varepsilon_0 \mu_0}}$ (m/s). P (C/m^2) and M (Wb/m^2) are the induced electric and magnetic polarization vectors, respectively. When we consider the optical fiber, the equations are further simplified because of the non-magnetic medium ($M = 0$), and the absence of free charges (ρ_f=0) and free current ($J = 0$). The wave equation that describes the propagation of light inside the fiber can be obtained by substituting Eq. (2.2) into Maxwell's equations and taking the curl of Eq. (2.1a), that leads to:

$$\nabla^2 E(r,t) - \frac{1}{c^2}\frac{\partial^2 E(r,t)}{\partial t^2} = \mu_0 \frac{\partial^2 [P_L(r,t) + P_{NL}(r,t)]}{\partial t^2} \tag{2.3}$$

where P_L and P_{NL} are the linear and the nonlinear components of the induced electric polarization defined as:

$$P_L(r,t) = \varepsilon_0 \int_{-\infty}^{\infty} \chi^{(1)}(t-t')E(r,t')dt' \tag{2.4}$$

$$\begin{aligned} P_{NL}(r,t) = \varepsilon_0 \left[\int_{-\infty}^{\infty}\int_{-\infty}^{\infty} \chi^{(2)}(t-t')E^2(r,t')dt'dt' \right] \\ + \varepsilon_0 \left[\int_{-\infty}^{\infty}\int_{-\infty}^{\infty}\int_{-\infty}^{\infty} \chi^{(3)}(t-t')E^3(r,t')dt'dt'dt' + \ldots \right] \end{aligned} \tag{2.5}$$

where $\chi^{(n)}$ is the nth order susceptibility of the dielectric medium. In Eq.(2.5), 2^{nd} order term vanishes due to inversion symmetry of silica fibers and the third order susceptibility $\chi^{(3)}$ becomes dominant that creates main nonlinear effects such as SPM and Raman scattering [11]. Thus, P_L and P_{NL} are approximated as:

$$P_L = \varepsilon_0 \chi^{(1)} E(r,t) \tag{2.6a}$$

$$P_{NL} \approx \varepsilon_0 \varepsilon_{NL} E(r,t) \tag{2.6b}$$

where

$$\varepsilon_{NL} = \frac{3}{4}\chi^{(3)}|E(r,t)|^2 \tag{2.6c}$$

The following assumptions are made in order to solve the wave equation in Eq.(2.3) [11]:

i The induced nonlinear polarization (P_{NL}) is so weak (causes less than 10^{-6} refractive index change), hence treated as a small perturbation.

ii The polarization is preserved along the fiber.

iii Slowly varying envelope approximation is used, because the field is quasi-monochromatic ($\Delta\omega/\omega_0 \ll 1$), where $\Delta\omega$ (Hz) is the bandwidth of the field and ω_0 (Hz) is the central frequency.

The propagation equation Eq.(2.3) fits better in the Fourier domain after simplifications and transforms to:

$$\nabla^2 E(r,\omega) + \varepsilon(\omega)k_0^2 E(r,\omega) = 0 \tag{2.7}$$

where the complex permittivity $\varepsilon(\omega) = \varepsilon_0(1 + \tilde{\chi}^{(1)}(\omega) + \tilde{\chi}^{(3)}(\omega) + \tilde{\chi}^{(5)}(\omega) + \ldots)$, $\tilde{\chi}^{(n)}$ is the Fourier transform of $\chi^{(n)}$ and the wavenumber $k_0 = \omega_0/c$ (rad/m). The refractive index (n) and the absorbtion coefficient (α) can be derived from the dielectric constant via

$$\varepsilon = \left(n + i\frac{\alpha}{2k_0}\right)^2 = (n_L + \Delta n)^2 \tag{2.8}$$

Therefore, they consist of both linear and nonlinear terms described by

$$n = n_L + n_{NL} = n_L + n_2|E|^2 \tag{2.9a}$$

$$\alpha = \alpha_L + \alpha_{NL} = \alpha_L + \alpha_2|E|^2 \tag{2.9b}$$

where the nonlinear index coefficient $n_2 = \frac{3}{8n}\Re\left[\chi^{(3)}\right]$ and two-photon absorption coefficient $\alpha_2 = \frac{3\omega_0}{4nc}\Im\left[\chi^{(3)}\right]$. The dielectric constant is mainly calculated by the refractive index and the absorption loss is added as a small perturbation as mentioned in the equation Eq. (2.8) where $\Delta n = n_2|E|^2 + i\frac{\alpha}{2k_0}$.

The separation of variables method can be used to solve Helmholtz Equation in Fourier domain and the solution will be in the form of:

$$E(r,\omega) = F(x,y)A(z,\omega)exp(i\beta_0 z) \tag{2.10}$$

where $F(x,y)$ is the field distribution of the fiber mode, $A(z,\omega)$ is the slowly varying envelope and the β_0 is the wave number. The mode distribution and the envelope equations can be derived from Eq.(2.7), when $E(r,\omega)$ terms replaced by the Eq.(2.10).

$$\frac{\partial^2 F(x,y)}{\partial x^2} + \frac{\partial^2 F(x,y)}{\partial y^2} + (\beta_0^2 - \bar{\beta}^2)F = 0 \tag{2.11}$$

$$2i\beta_0 \frac{\partial A}{\partial z} + (\bar{\beta}^2 - \beta_0^2)A = 0 \tag{2.12}$$

The first equation is solved by treating Δn as a first order perturbation, hence $\varepsilon = (n_L + \Delta n)^2 \approx n_L^2$. Therefore, $F(x,y)$ is independent of the nonlinear perturbation (Δn). The wave number is also defined as the sum of the linear and nonlinear terms respectively as in $\bar{\beta}(\omega) = \beta(\omega) + \Delta\beta(\omega)$.

$$\Delta\beta(\omega) = \frac{\omega^2 n(\omega)}{c\bar{\beta}(\omega)} \frac{\int_{-\infty}^{\infty}\int_{-\infty}^{\infty} \Delta n(\omega)|F(x,y)|^2 dxdy}{\int_{-\infty}^{\infty}\int_{-\infty}^{\infty} |F(x,y)|^2 dxdy} = i\frac{\alpha}{2} + \gamma|A|^2 \tag{2.13}$$

where $\gamma = \frac{n_2\omega_0}{cA_{eff}}$ is the nonlinear parameter and $A_{eff} = \frac{\left[\int_{-\infty}^{\infty}\int_{-\infty}^{\infty} |F(x,y)|^2 dxdy\right]^2}{\int_{-\infty}^{\infty}\int_{-\infty}^{\infty} |F(x,y)|^4 dxdy}$ is the effective mode area. The linear and nonlinear wave number terms are expanded by using Taylor expansion around the carrier frequency ω_0, as shown below.

$$\beta(\omega) = \beta_0 + \sum_{j=1}^{\infty} \frac{1}{j!}\beta_j(\omega - \omega_0)^j \tag{2.14a}$$

$$\Delta\beta(\omega) \approx \Delta\beta_0 \tag{2.14b}$$

$$\bar{\beta}(\omega) \approx \beta_0 + \sum_{j=1}^{\infty} \frac{1}{j!}\beta_j(\omega - \omega_0)^j + \Delta\beta_0 \tag{2.14c}$$

where β_j is the jth order linear dispersive term and $\Delta\beta_0$ is the zeroth order nonlinear term.

By using the approximation $(\bar{\beta}^2 - \beta_0^2) \approx 2\beta_0 \left[\bar{\beta}(\omega) - \beta_0\right]$ and substituting $\bar{\beta}(\omega)$ with Eq.(2.14c), Eq.(2.12) simplifies to [12]

$$\frac{\partial A}{\partial z} - i\sum_{j=1}^{\infty} \frac{1}{j!}\beta_j(\omega - \omega_0)^j A = i\Delta\beta_0 A \tag{2.15}$$

Further by substituting $\Delta\beta_0$ with $i\frac{\alpha}{2} + \gamma|A|^2$ and taking the inverse Fourier transform of both sides of Eq. (2.15), the well known Nonlinear Schrödinger Equation (NLSE) for A(z,t) is derived as:

$$\frac{\partial A}{\partial z} + \sum_{j=1}^{\infty} \frac{-i^{j+1}}{j!}\beta_j \frac{\partial^j A}{\partial t^j} = -\frac{\alpha}{2}A + i\gamma(\omega_0)|A|^2 A \tag{2.16}$$

The NLSE simplifies to

$$\frac{\partial A}{\partial z} + \beta_1\frac{\partial A}{\partial t} + i\frac{1}{2}\beta_2\frac{\partial^2 A}{\partial t^2} - \frac{1}{6}\beta_3\frac{\partial^3 A}{\partial t^3} + \frac{\alpha}{2}A = i\gamma|A|^2 A \tag{2.17}$$

after neglecting the higher order dispersion ($\beta_j = 0, j > 3$).

The simplified NLS equation (Eq. (2.17)) includes the effects of group velocity, group velocity dispersion, GVD slope, fiber loss, and fiber non-linearity respectively. The β_1 (s/m) is the reciprocal of group velocity and the β_2 (ps^2/km) is the GVD parameter of the propagation medium. GVD slope (β_3) is negligibly small, unless second order dispersion is $\sim$0 [11].

2.1.2 Group Velocity Dispersion

Group velocity is defined as the effective velocity of a wave packet that includes several frequency components. In an optical dispersive medium, the lights with different colors (frequencies) travel at different velocity. Since speed is associated with the refractive index, dispersion means having different refractive indices for different colors. In bulk materials dispersion is a material property. In fibers, the net dispersion has two parts: material and waveguide dispersion that are originated from the nature of the material used to propagate light and the optical waveguide design such as its geometry and materials used in core and cladding parts. In an optical fiber, phase velocity can be defined as $\nu_g = c/n(\omega)$ in terms of frequency. Generally, there are two types of dispersion such as normal and anomalous. In normal dispersion, the lower frequencies (red shifted) travel

faster than higher frequencies (blue shifted) and it is vice versa for anomalous dispersion. The optical wave starts to broaden because of the speed difference between different frequency components. The effect of GVD on the pulse propagation in a linear medium can be studied by eliminating all the nonlinear terms in Schrödinger equation, which results to a simplified NLSE:

$$i\frac{\partial A}{\partial z} = -\frac{\beta_2}{2}\frac{\partial^2 A}{\partial t^2} \tag{2.18}$$

This simplified differential equation can easily be solved by Fourier transform method. The normalized, arbitrary shaped pulse in time domain $A(z,t)$ and its spectrum $\hat{A}(z,\omega)$ in frequency domain are related by Fourier transform as:

$$A(z,t) = \frac{1}{2\pi}\int_{-\infty}^{\infty} \hat{A}(z,\omega)\exp(-i\omega t)d\omega \tag{2.19}$$

By taking the Fourier transform of both sides in Eq. (2.18) with using time derivative property $\left(\frac{\partial^n}{\partial t^n} \rightarrow (i\omega)^n\right)$, it transforms into an ordinary differential equation:

$$i\frac{\partial \hat{A}}{\partial z} = -\frac{1}{2}\beta_2\omega^2\hat{A} \tag{2.20}$$

which has a solution in the form of:

$$\hat{A}(z,\omega) = \hat{A}(0,\omega)\exp\left(\frac{i}{2}\beta_2\omega^2 z\right) \tag{2.21}$$

It is obvious from the solution that GVD alters only the phase, not the amplitude of the initial pulse spectrum. The added phase is proportional to the frequency and propagation length. The phase change in spectrum modifies the pulse shape in time domain as shown in Fig. 2.1. The corresponding time domain solution is evaluated by taking the inverse Fourier Transform of Eq. (2.21).

$$A(z,t) = \frac{1}{2\pi}\int_{-\infty}^{\infty} \hat{A}(0,\omega)\exp\left(\frac{i}{2}\beta_2\omega^2 z\right)\exp(i\omega t)d\omega \tag{2.22}$$

The femtosecond laser pulses used in optics do not have a well-defined shape due to nonlinear processes inside the laser cavity, distortions, and noise interference etc. However, they can be approximated as Gaussian pulses, which are well defined mathematically, in order to investigate the effect of optical system on the pulse. The following part is the review on the effect of GVD on the Gaussian pulses. A normalized Gaussian pulse

defines the initial pulse:

$$A(0,t) = \exp\left[\frac{1+iC}{2}\left(\frac{t}{T_0}\right)^2\right] \tag{2.23}$$

where C is the initial chirp parameter and T_0 is the half width at $1/e$ intensity point and related to full width at half maximum as $T_{FWHM} = 1.665T_0$. The final pulse after propagation becomes:

$$A(z,t) = \frac{T_0}{\sqrt{T_0^2 - i\beta_2 z(1+iC)}} \exp\left[-\frac{(1+iC)t^2}{2(T_0^2 - i\beta_2 z(1+iC))}\right] \tag{2.24}$$

The result shows that both initially chirped ($C \neq 0$) and unchirped ($C = 0$) Gaussian pulses conserve their Gaussian shapes after propagation. However, the pulse width T_1 (defined similar to T_0) and the chirp parameter C_1 of the pulse change due to GVD as [13]:

$$\frac{T_1}{T_0} = \left[1 + \left(\frac{C\beta_2 z}{T_0^2}\right)^2 + \left(\frac{\beta_2 z}{T_0^2}\right)^2\right]^{1/2} \tag{2.25}$$

$$C_1(z) = C + (1+C^2)\frac{\beta_2 z}{T_0^2} \tag{2.26}$$

According to the results, it is easily seen that, if there is no initial chirp on the pulse, the pulse starts to broaden due to GVD independent of the medium type such as normal ($\beta_2 > 0$) or anomalous ($\beta_2 < 0$). If there is an initial chirp, pulse broadens faster than unchirped case when $\beta_2 C > 0$. On the other hand, if $\beta_2 C < 0$, the pulse first compress to compensate the effect of initial chirp and then starts to broaden again [13].

Simulation Results

The following simulation results show the GVD effect on the Gaussian pulse in time and frequency domain. The results are obtained by using SSFM with zero nonlinearity.

Figure 2.1 and 2.2 show the evolution of transform limited and chirped Gaussian pulses along the fiber under the effect of GVD respectively. In the figures, the propagating pulses are displayed only at specific distances that are multiples of dispersion length, $L_D = \frac{T_0^2}{|\beta_2|}$, to indicate the broadening and compression effects. Additionally, such pulses are normalized according to the peak intensity of the initial pulse. It is clearly seen in Fig. 2.1 that the GVD does not affect the spectrum intensity. However, time domain pulses are broadened due to phase change in the frequency domain. On the other hand,

Fig. 2.2 demonstrates initially chirped pulse propagation where compression and faster broadening properties are observed. In addition to these, it is seen that Gaussian pulses remain Gaussian after propagation in linear dispersive mediums.

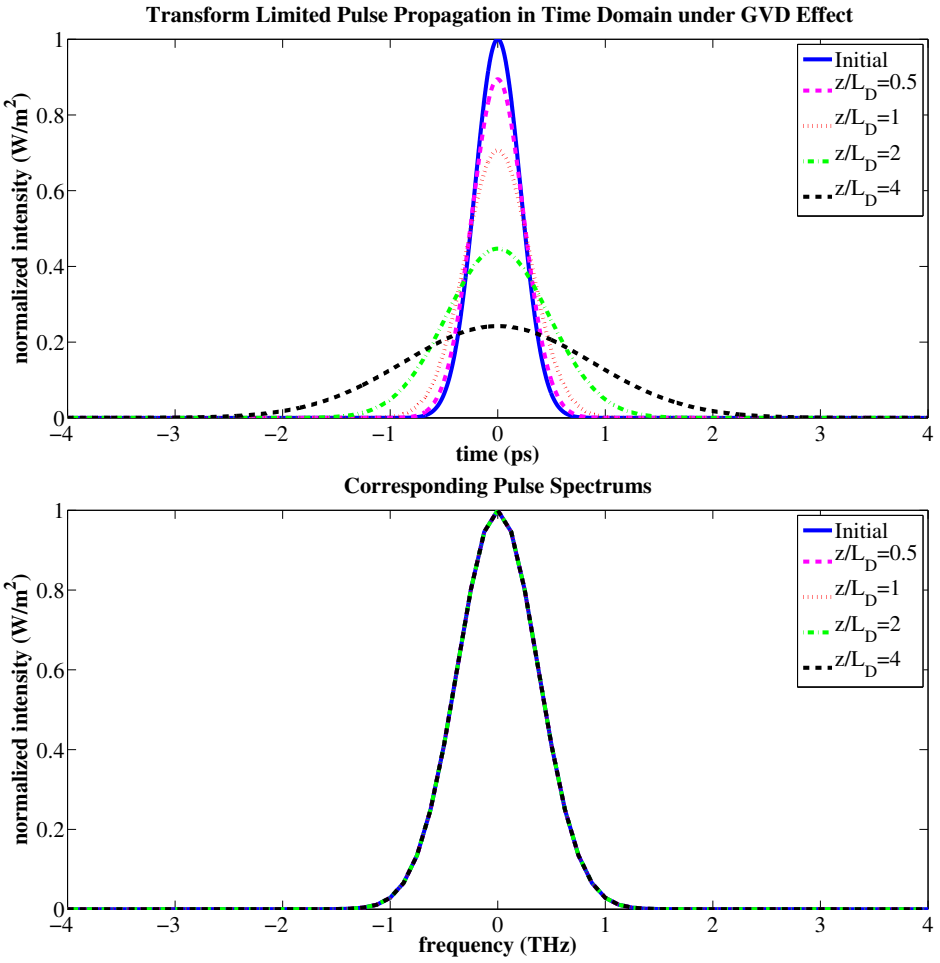

FIGURE 2.1: Transform limited Gaussian pulse ($T_{FWHM} = 500fs$) propagation inside a fiber. Temporal (upper) and Spectral (down) evolution due to GVD (D=17 ps/km-nm).

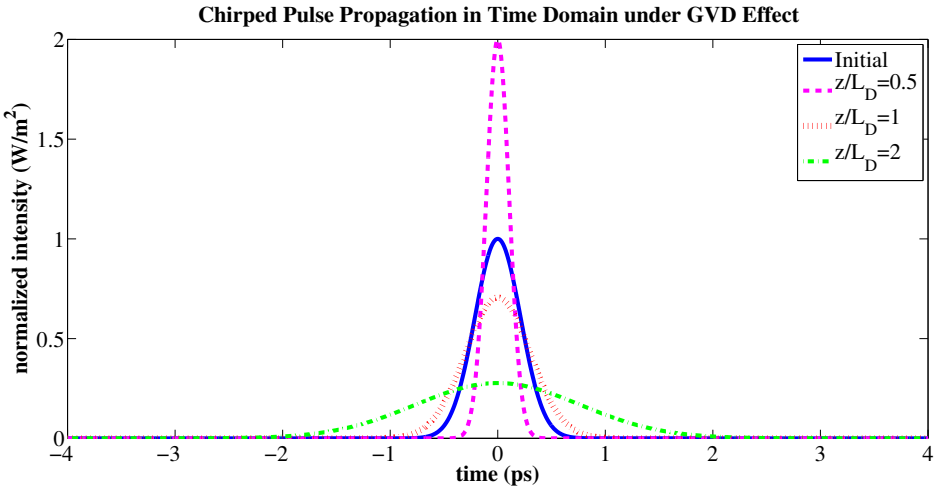

FIGURE 2.2: Chirped Gaussian pulse ($C = 2$) propagation inside a fiber under the effect of GVD (β_2=-21.67 ps^2/km). $L_D = \frac{T_0^2}{|\beta_2|}$ is the dispersion length.

2.1.3 Nonlinear Optical Effects

The optical medium becomes nonlinear, when the electromagnetic field (light) intensity increases due to small core area of the fiber and high peak power of the ultra short pulses. Self and Cross Phase Modulation (SPM/XPM) are two fundamental nonlinear effects.

2.1.3.1 Self Phase Modulation

Refractive index of the dielectric medium also depends on the intensity of the light, in addition to the frequency as in GVD. The refractive index profile becomes nonlinear, when the light intensity inside the medium increases. As a result, the pulse experiences both linear GVD and nonlinear effects while propagating in fiber. The comparison between the dispersion and nonlinear length determines the dominant effect.

$$L_D = \frac{T_0^2}{|\beta_2|} \tag{2.27a}$$

$$L_{NL} = \frac{1}{\gamma P_0} \tag{2.27b}$$

where L_D, L_{NL} are dispersion and nonlinear lengths respectively, γ is the nonlinearity parameter and P_0 is the peak power of the pulse [11]. Three possible cases are shown below.

i) If $L > L_D$ and $L > L_{NL}$, both GVD and SPM is effective.

ii) If $L_D \gg L > L_{NL}$, then GVD is negligible.

iii) If $L_{NL} \gg L > L_D$, then SPM is negligible.

Therefore, the individual effect of SPM can be studied by eliminating GVD in NLS Equation (case 2). The equation simplifies to

$$\frac{\partial A}{\partial z} = ie^{-\alpha z}\gamma P_0 |A|^2 A \tag{2.28}$$

As it is seen in Eq. (2.28), SPM creates an intensity dependent nonlinear phase on the pulse without changing the pulse shape in time domain. However, the added phases would distort the spectrum drastically. The solution to the above ordinary differential equation is

$$A(z = L, t) = A(0, t)\exp[i\phi_{NL}(z = L, t)] \tag{2.29}$$

where $\phi_{NL}(L, t) = |A(0, t)|^2 \gamma P_0 L_{eff}$ is the nonlinear phase and $L_{eff} = \frac{1-\exp(-\alpha L)}{\alpha}$ is the effective length. The maximum phase shift occurs at the peak intensity point (center for the Gaussian pulses) and given by $\phi_{max} = \gamma P_0 L_{eff}$.

Any time dependent phase on the signal creates new frequency components in the spectrum as it is stated in Fourier Theorem. In other words, phase change across the pulse creates an instantaneous frequency deviation from the center value ω_0 that causes a spectral broadening. The amount of SPM induced spectral shift, also called frequency chirp ($\delta\omega$) is obtained by taking the derivative of nonlinear phase.

$$\delta\omega(t) = -\frac{\partial \phi_{NL}}{\partial t} = -\gamma P_0 L_{eff} \frac{\partial}{\partial t}|A(0, t)|^2 \tag{2.30}$$

For Gaussian pulses as in Eq. (2.23), the SPM induced frequency shift is:

$$\delta\omega(t) = -\frac{2}{T_0^2}\frac{L_{eff}}{L_{NL}} t \exp\left(-\frac{t^2}{T_0^2}\right) \tag{2.31}$$

with a maximum shift of $\delta\omega_{max} = 0.86\Delta\omega_0\phi_{max}$ where $\Delta\omega_0 = T_0^{-1}$.

Simulation Results

The effect of Self Phase Modulation both in time and frequency domains is shown in the following simulation results. The input pulse is again taken as the normalized Gaussian pulse. We can see that the spectrum is drastically distorted, while the pulse shape is conserved through the propagation, as mentioned before. The results are obtained by using SSFM with changing parameters to satisfy case 2 ($L_D \gg L > L_{NL}$).

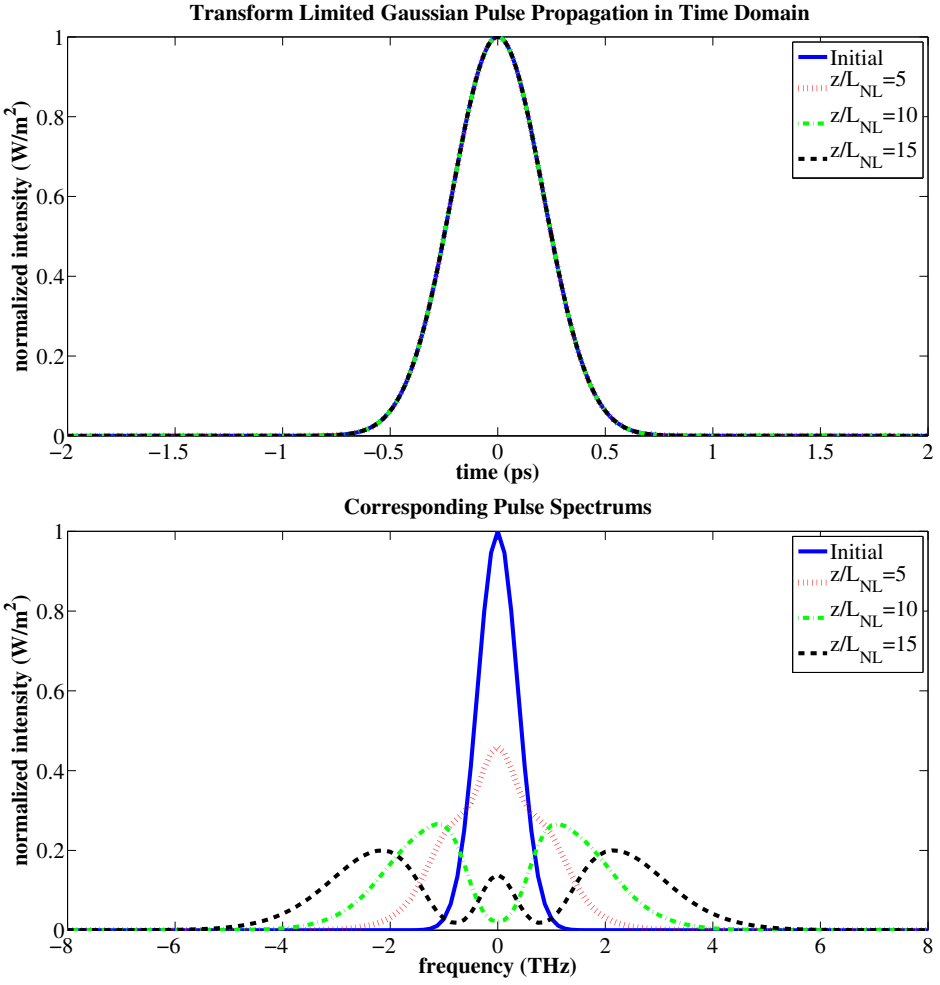

FIGURE 2.3: Transform limited Gaussian pulse propagation inside the fiber. Temporal (upper) and spectral (down) evolution due to nonlinear effect ($\gamma = 2W^{-1}km^{-1}$).

The SPM makes spectral change, while preserving the time domain signals as opposed to GVD. As it is shown in Fig. 2.3, the SPM is nonlinear and it transforms the spectrum arbitrarily.

2.1.3.2 Cross Phase Modulation

Cross Phase Modulation is another nonlinear phenomenon similar to SPM, occurs when there are more than one optical beam in the medium at the same time. When the beams interact with each other, each optical beam experiences a refractive index change affected by its own intensity and the intensity of other beams that causes spectral broadening of the pulses [11]. The nonlinear phase caused by XPM is twice as high as SPM for the same intensity. As a result, the total nonlinear phase seen by each pulse due to SPM and XPM when N optical pulses with different frequencies propagate in a medium becomes [13]:

$$\varphi_j(t) = \gamma_j \left[L|A_j(0,t)|^2 + 2\sum_{j\neq k} \int_0^L |A_k(0, t - zd)|^2 dz \right] \tag{2.32}$$

where $j = 1 - N$. As seen in the above equation, XPM is also dependent to the relative positions of the pulses $(t - zd)$. The pulses only overlap in a certain time window, because they travel at different velocities in a dispersive medium. The walk-off between the pulses affects the amount of the spectral broadening due to XPM [14].

2.2 Numerical solutions to Nonlinear Schrödinger Equation

The full wave Maxwell equation does not generally have any analytical solution in nonlinear optical medium. Additionally, numerical solutions are very hard to apply due to dimensionality problem. However, an approximate solution can be found by using some predefined conditions and assumptions. There are simply two kinds of numerical methods such as pseudo spectral and finite difference methods that differ in terms of putting the carrier frequency into the account or not. The finite difference methods include the carrier frequency, they can calculate forward and backward propagating waves more accurately than pseudo-spectral methods [15]. Split Step Fourier Method is one of the pseudo-spectral numerical methods that is extensively used to solve NLS equation for the propagation of pulses because of its easy implementation and fast computation [11]. In this study, I utilized SSFM method to investigate the pulse propagation inside the fiber.

2.2.1 Split Step Fourier Method

The fundamental idea of the SSFM is that the linear and nonlinear parts of NLS equation are treated separately using the analytical solutions of individual parts. Even though NLSE does not have any analytical solution, the individual linear and nonlinear parts have. They can be solved separately with a small numerical error by dividing the propagation distance into small steps (h). As a summary, the linear term due to GVD and nonlinear term due to SPM are defined respectively as [15]:

$$D = -\frac{\alpha}{2} - \sum_{m=2}^{3} \frac{i^{m-1}}{m!}\beta_m \frac{\partial^m}{\partial T^m} \tag{2.33a}$$

$$N = i\gamma \left[|A(z,t)|^2 + \frac{i}{\omega_0 A(z,t)} \frac{\partial}{\partial t}[|A(z,t)|^2 A(z,t)] \right] \tag{2.33b}$$

where $A(z,t)$ is the complex field envelope at distance (z) and time (t). Thus the NLS equation can be written in the form as [15, 16]:

$$\frac{\partial A(z,t)}{\partial z} = (D+N)A(z,t) \tag{2.34}$$

with a general solution of

$$A(z+h,t) = \exp[h(D+N)]A(z,t) \tag{2.35}$$

The solution is approximated by adding the dispersive and nonlinear effects independently over small distance (h) which is divided into two.

$$\exp[h(D+N)] = \exp(hD)\exp(hN) \tag{2.36}$$

The dispersion (D) effect is analyzed in frequency domain, since multiplication is computationally less complex than taking derivative in time domain. Thus, taking the Fourier Transform of both sides by using differentiation theorem, so NLS equation reduces to [15, 16]:

$$\frac{\partial A(z,\omega)}{\partial z} = -\frac{\alpha}{2}A(z,\omega) - \sum_{m=2}^{3} \frac{i^{m-1}}{m!}\beta_m (i\omega)^m A(z,\omega) \tag{2.37}$$

with the solution of

$$A(z+h,\omega) = A(z,\omega)\exp\left\{h\left[-\frac{\alpha}{2} - \sum_{m=2}^{3}\frac{i^{m-1}}{m!}\beta_m(i\omega)^m\right]\right\} \tag{2.38a}$$

$$A(z+h,t) = \mathcal{F}^{-1}\left\{A(z+h,\omega)\right\} \tag{2.38b}$$

In order to reduce the error accumulation more, we employed a modified technique called symmetrized SSFM in our simulations. The general procedure applied in symmetrized SSFM at every h distance is shown step by step below [15, 16]:

i) Dispersion and loss is calculated over h/2 by setting N=0.

$$A\left(z+\frac{h}{2},T\right) = \mathcal{F}^{-1}\left\{\exp\left[\frac{h}{2}D(i\omega)\right]\mathcal{F}\left\{A(z,T)\right\}\right\}$$

ii) At the midpoint of step size, nonlinearity is calculated by setting D=0.

$$A\left(z+\frac{h}{2},T\right) = A\left(z+\frac{h}{2},T\right)\exp(hN)$$

iii) Dispersion and loss is calculated over the second half by setting N=0.

$$A\left(z+h,T\right) = \mathcal{F}^{-1}\left\{\exp\left[\frac{h}{2}D(i\omega)\right]\mathcal{F}\left\{A(z+\frac{h}{2},T)\right\}\right\}$$

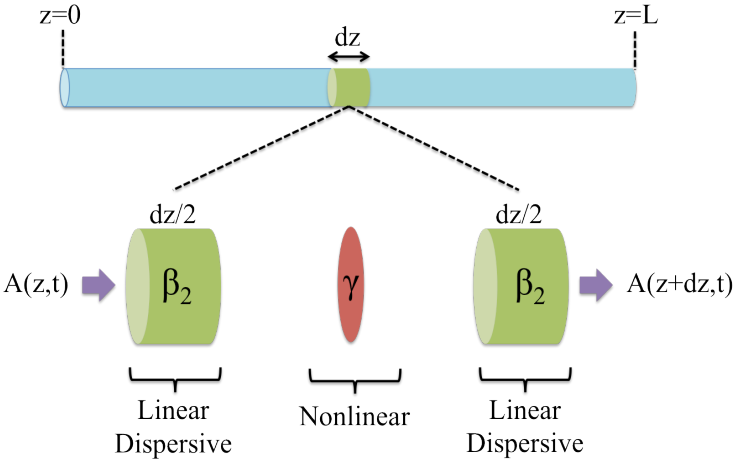

FIGURE 2.4: Schematic of Split Step Fourier Method [16].

2.3 Optical Solitons

Soliton is defined as a self-reinforcing solitary wave that conserves its shape while propagating at a constant speed. In optics, the solitons preserve their shape and survive after collisions in a nonlinear medium due to the balance between dispersion and SPM. Solitons' most outstanding feature is distortionless propagation that facilitates the usage in long-haul optical communication systems [13].

In this study, I used optical solitons to verify that my MATLAB codes related to SSFM are working perfect with using their property of self recovery. Therefore, the initial and final pulse shapes are compared as shown in Table 2.1.

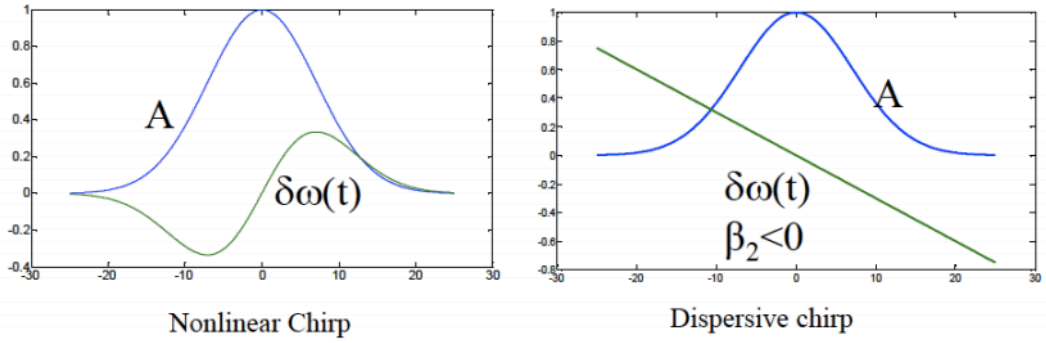

FIGURE 2.5: Nonlinear and Dispersive Chirps [12].

Dispersion and SPM cancel the effect of each other mainly at the center of the pulse, as shown in Fig. 2.5, when they simultaneously affect the pulse in a fiber. As mentioned earlier, GVD is a linear dispersive effect that broadens the transform-limited ($C = 0$) optical pulse. On the other hand, SPM as a dominant nonlinear effect introduces a positive chirp ($C > 0$) on the propagating pulse. Therefore, soliton can be formed in anomalous dispersion regime ($\beta_2 < 0$) in order to balance the broadening effect of SPM ($\beta_2 C < 0$ case) mainly in the central part of the pulse. In order to get fully balanced soliton, the SPM induced chirp can be tuned by altering peak power [13].

In other words, GVD effect moves the lower frequency components (red) to the front edge due to faster propagation in anomalous dispersive regime, and SPM shifts them backwards with propagating them slowly. As a result, when the two shifts are balanced and the pulses come back to their original positions after both effects (zero chirp), the undistorted soliton propagation can be achieved.

With all these explanations we can state that soliton is a solution of nonlinear Schrödinger equation for lossless medium when XPM and higher order nonlinearities are not present, that is

$$\frac{\partial A}{\partial z} + i\frac{\beta_2}{2}\frac{\partial^2 A}{\partial t^2} = i\gamma|A|^2 A \tag{2.39}$$

With substitutions $\tau = \frac{t}{T_0}$, $\xi = \frac{z}{L_D}$ and $u = N\frac{A}{\sqrt{P_0}}$ where T_0 is the pulse width, P_0 is the peak power and $L_D = \frac{T_0^2}{|\beta_2|}$ is the dispersion length, the Eq. (2.39) transforms to [11]:

$$i\frac{\partial u}{\partial \xi} + \frac{1}{2}\frac{\partial^2 u}{\partial \tau^2} + |u|^2 u = 0 \tag{2.40}$$

The above equation is a special class of nonlinear differential equations that can be solved by inverse scattering method and the solution can be the soliton wave, namely hyperbolic secant pulses. The normalized NLS equation states that hyperbolic secant pulses, may be formulated as $u(0,\tau) = Nsech(N\tau)$ at the beginning of the propagation, repeats the shape periodically at every $\xi = m\frac{\pi}{2}$ and distance $z_0 = \frac{\pi}{2}L_D$ [11]. Additionally, the parameter N determines the propagation pattern. The fundamental soliton ($N = 1$) can propagate without changing its shape. However, the higher order solitons ($N > 1$) follow a periodic pattern and restore its initial features such as amplitude, pulse shape and width at the soliton period (z_0) and its multiples. The parameter N has a physical meaning which is related with the dispersion and nonlinear lengths formulated as $N^2 = \frac{L_D}{L_{NL}}$. For higher order solitons ($N > 3$), dispersion length becomes so much higher than nonlinear length, thus GVD becomes almost negligible and SPM dominates.

2.3.1 Soliton Propagation and Simulation Results

Soliton propagation inside a lossless fiber is investigated for different soliton-orders up to three and the results are compared with the theoretical ones to verify the reliability of the MATLAB codes.

In the fundamental soliton case ($L_D = L_{NL}$), we observed the undistorted propagation inside the lossless fiber as seen in Fig. 2.6 by choosing the pulse width and the peak power appropriately such as $P_0 = \frac{|\beta_2|}{\gamma T_0^2}$.

It is demonstrated in Fig. 2.6 that the pulse width stays same along the propagation. The maximum distortion (error) between initial and final ($z = z_0$) pulses is calculated

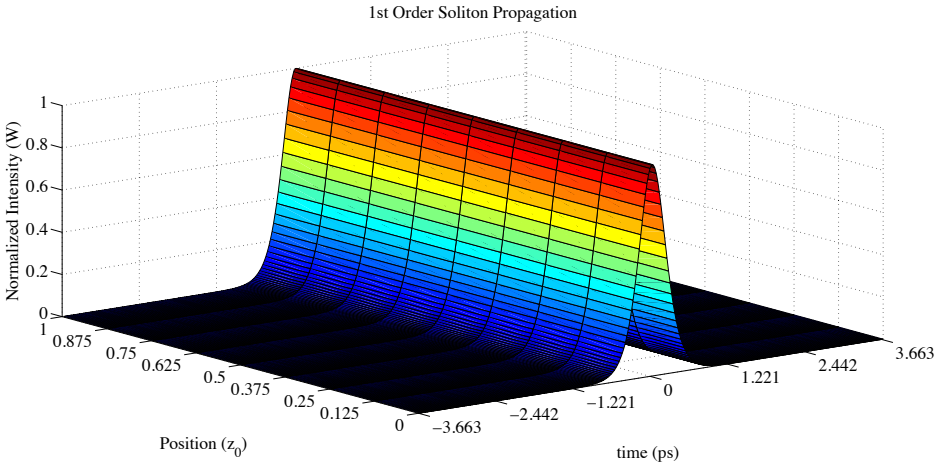

FIGURE 2.6: Fundamental Soliton pulse evolution in a fiber.

as 0.0688%, however it accumulates to 0.1171% after ten times longer propagation ($L = 10z_0$). The maximum error values are tabulated for higher order solitons in Table 2.1.

However, for the higher-order soliton case, the situation is completely different. Soliton pulses chosen such that $N > 1$, propagate by changing their shapes, pulse widths and peak powers periodically. In fact, this periodicity occurs for all higher-order solitons. At every $\xi = m\frac{\pi}{2}$ distance, soliton recovers its original shape. This pattern is repeated over each section of soliton period which is defined as $z_0 = \frac{\pi}{2}L_D$.

For the second order case, as seen in Fig. 2.7, soliton contracts to a fraction of its initial pulse width and merges again to its original shape.

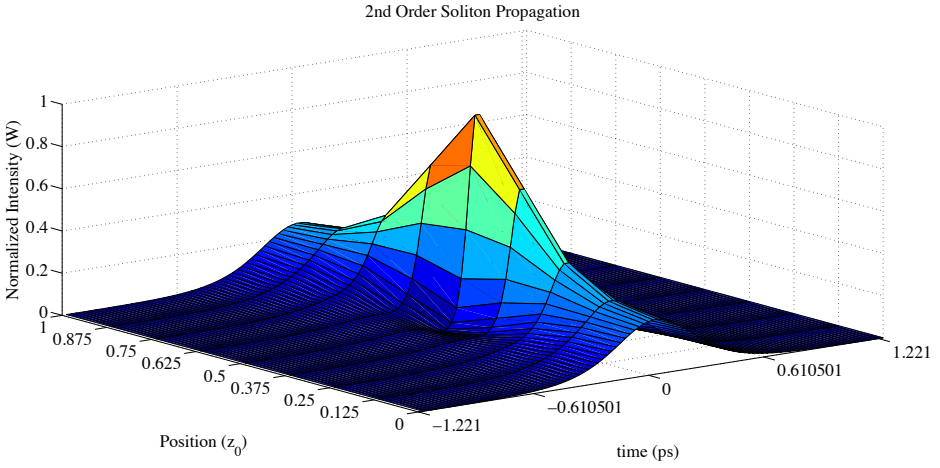

FIGURE 2.7: Second order Soliton pulse evolution in a fiber.

For the third order case, as seen in Fig. 2.8, soliton first compresses, splits into two distinct pulses at the half period and merges again to its original shape.

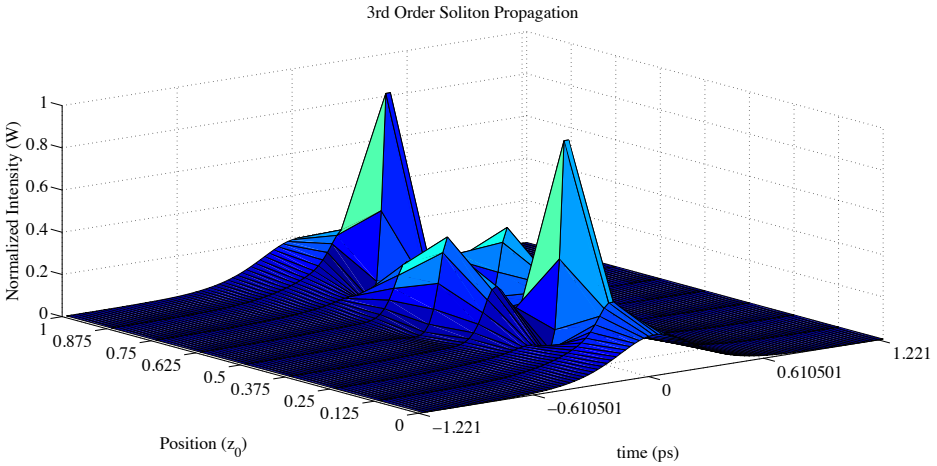

FIGURE 2.8: Third order Soliton pulse evolution in a fiber.

TABLE 2.1: Maximum percentage errors for up to 3^{rd} order soliton.

Soliton Order	Maximum error at L=z_0	Maximum error at L=10z_0
N=1	0.0688%	0.1171%
N=2	0.0680%	0.1245%
N=3	0.1299%	15.2701%

As it is obviously seen in the Table 2.1, the only problematic value exists for 3^{rd} order soliton after the propagation length of $L = 10z_0$. Such high errors may be caused by the inadequate step size that could not put the SPM effect into account efficiently. Thus, the balanced propagation is deteriorated. The input and output pulses for this case are shown in Fig. 2.9.

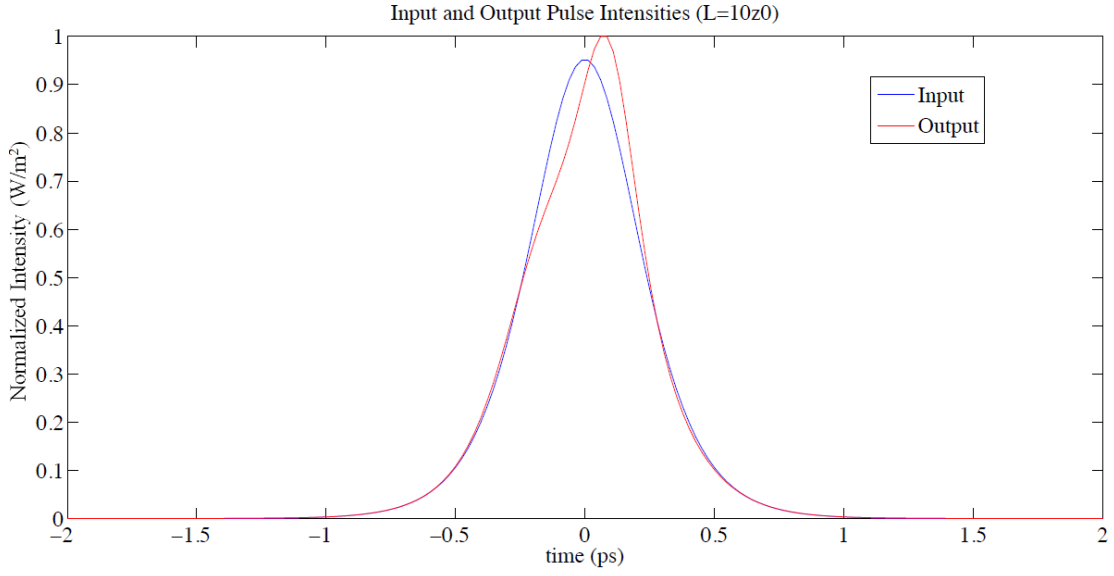

FIGURE 2.9: Third order Soliton pulse could not retain its shape completely at $L = 10z_0$.

2.3.2 Perturbation of Soliton

Soliton pulses propagate by retaining their shapes in a lossless fiber where only the GVD and SPM effects are included. However, in real life, other impacts such as fiber loss, thus amplification via stimulated Raman scattering will be present in NLS equation. These effects can be treated as small perturbations in NLS Equation, which will transform to [11]:

$$i\frac{\partial u}{\partial \xi} + \frac{1}{2}\frac{\partial^2 u}{\partial \tau^2} + |u|^2 u = i\varepsilon(u) \tag{2.41}$$

where $\varepsilon(u)$ represents the small perturbation that is a function of u [11]. The Eq. (2.41) can only be solved by assuming the functional form of Soliton solution remains same with different parameters. Therefore, the solution for perturbed NLS equation will be:

$$u(\xi, t) = \eta(\xi) sech[\eta(\xi)(\tau - q(\xi))] \exp[i\phi(\xi) - i\delta(\xi)\tau] \tag{2.42}$$

where η, δ, q, ϕ are defined as the amplitude, frequency, position and the phase parameters of the soliton and all depend on the propagation distance. The perturbation changes these Soliton parameters that evolves according to the following set of equations, which can be solved by using variational method.

$$\frac{d\eta}{d\xi} = \Re\left\{\int_{-\infty}^{\infty} \varepsilon(u) u^*(\tau) d\tau\right\} \tag{2.43a}$$

$$\frac{d\eta}{d\xi} = -\Im\left\{\int_{-\infty}^{\infty} \varepsilon(u) tanh[\eta(\tau - q)] u^*(\tau) d\tau\right\} \tag{2.43b}$$

$$\frac{d\eta}{d\xi} = -\delta + \frac{1}{\eta^2}\int_{-\infty}^{\infty} \varepsilon(u)(\tau - q) u^*(\tau) d\tau \tag{2.43c}$$

$$\frac{d\eta}{d\xi} = \Im\left\{\int_{-\infty}^{\infty} \varepsilon(u)\left\{\frac{1}{\eta} - (\tau - q)tanh[\eta(\tau - q)]\right\} u^*(\tau) d\tau + \frac{1}{2}(\eta^2 - \delta^2) + q\frac{d\delta}{d\xi}\right\} \tag{2.43d}$$

where $\Re$ and $\Im$ represent the real and imaginary parts respectively [17].

When the loss is accounted in the fiber, the balance between GVD and SPM breaks, since the decreased peak power along the fiber will diminish the SPM effect. In order to rebalance the system, broadening effect due to GVD will be reduced by increasing the pulse width, as given earlier in Eq. (2.25). The fiber losses can be modeled as $i\varepsilon(u) = -\frac{i}{2}\Gamma u$ where $\Gamma = \alpha L_D$ and the analytical solution shows that only the amplitude

and phase parameters are modified due to the perturbation caused by fiber losses.

$$\eta(\varepsilon) = \eta(0)\exp(-\Gamma\xi) \tag{2.44a}$$

$$\phi(\xi) = \phi(0) + \frac{1-\exp(-2\Gamma\xi)}{4\Gamma} \tag{2.44b}$$

The final pulse width becomes $T_1 = T_0\exp(-\Gamma\xi)$ due to inverse proportionality between the pulse width T_0 and the amplitude $\eta(\varepsilon)$ [18].

Soliton amplification, which is literally the opposite of the loss, can also be modeled as a perturbation. Simply, there are two different soliton amplification schemes such as lumped and distributed. In the lumped case, soliton pulses are amplified abruptly after propagating certain distance, i.e. 40-60 km. After the amplification, the peak power will be so high and distort the pulse. However, the pulses will start to adjust themselves with dispersing some energy to a broadened time window to decrease peak power, hence to maintain the initial shape. If the amplification period L_A is comparable to the dispersion length L_D, soliton pulses break up and to release the extra energy as dispersive waves. Therefore, the amplification length should be much less than the dispersion length ($L_A \ll L_D$) to prevent breaking up [19]. The condition is not generally valid for lumped amplification; so distributed amplification is required. In ideal case, the amplification will be uniform through the fiber and just compensate the loss without any additional gain.

2.4 Stimulated Raman Scattering

In molecular mediums, there is another nonlinear process called Stimulated Raman Scattering that is widely employed in optics to operate optical fibers as an amplifier or tunable laser by transferring energy from one beam (pump) to others (Stokes) [20]. In other words, the weak Stokes wave that has lower frequency ($E = h\nu$), thus higher wavelength ($\lambda = \upsilon_p/f$), is amplified by the intense (higher frequency) pump beam via SRS process. The vibrational energy states in the medium, as shown in Fig 2.10, determines the amount of energy transfer between incident and scattered fields.

The pump wave begins to amplify Stokes wave due to Raman induced energy transfer; when both the pump and probe (Stokes) waves simultaneously propagate inside a fiber.

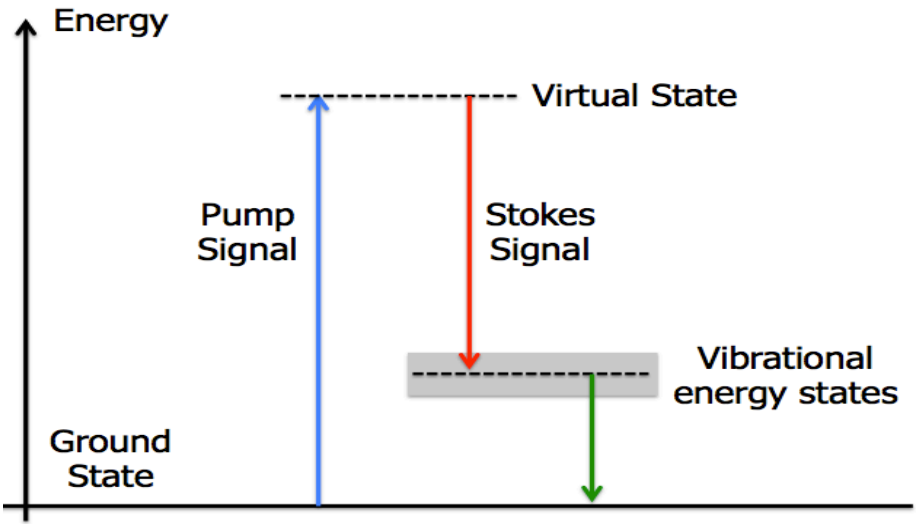

FIGURE 2.10: Energy Diagram of Raman Scattering [21].

This amplification process is governed by the following equation in a lossless medium:

$$\frac{\partial I_S}{\partial z} = g_R I_P I_S \tag{2.45}$$

where I_S and I_P are Stokes and pump waves respectively and g_R is the Raman gain coefficient [22], which is a function of frequency shift ($\Omega = \omega_P - \omega_S$) between the pump and Stokes waves, and depends on the composition of the fiber core, relative polarization of both fields (co-polarized or orthogonally polarized) and inversely proportional to the pump wavelength [23]. The silica fibers has a very wide Raman gain spectrum up to 40THz due to its amorphous nature. As it is seen in co-polarized case of Fig. 2.11b, the first peak is nearly at 13.2THz and the second peak is at 14.7THz due to non-crystalline nature of silica glass [11]. The multiple peaks exist, since several vibrational modes contribute to the gain spectra. However, the spectra can be modeled by a single peaked function like polynomial, Gaussian or Lorentzian with the loss of some fine structures [24].

As it is mentioned earlier, the stimulated Raman scattering occurs when both pump and probe beams propagate at the same time. The amplification lasts until the frequency shift lies inside the bandwidth of gain spectra. On the other hand, new frequency components can be generated and amplified by spontaneous Raman scattering, even the initial probe beam does not exist. Although photons within the 40THz bandwidth are generated and amplified, the frequency component which experiences the maximum Raman gain dominates the system due to higher amplification. As a result, in silica fibers, nearly

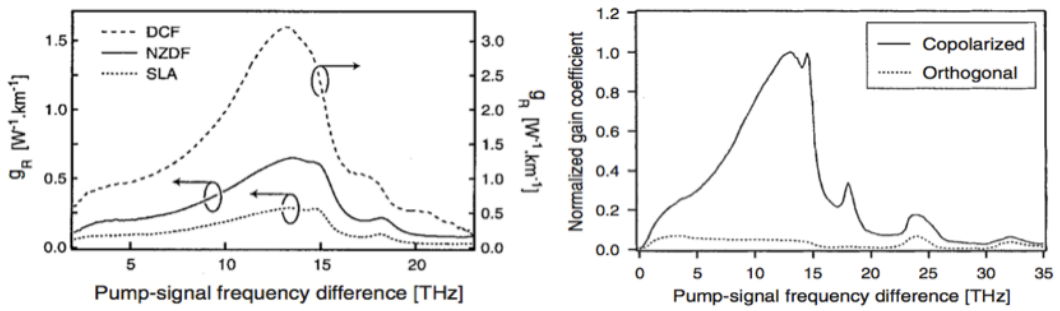

FIGURE 2.11: Raman gain spectrum of silica fiber and the effect of intensity (a), which depends on the type of fibers and the polarization states (b) on Raman gain coefficient [24].

13.2 THz downshifted Stokes wave is generated. The technique enables to generate 26.4-29.4THz (~1000cm^{-1}) frequency separated second order Stokes pulses with ~3THz (~40nm) tunability. This property leads to the design of multi wavelength stable soliton Raman lasers.

For the simplest case, the signal is pumped by single continuous wave (CW) laser, the evolution of pump and the probe beams is governed by the following equations including both the fiber losses and the interaction between them through SRS process [11].

$$\frac{\partial I_S}{\partial z} = g_R I_P I_S - \alpha_S I_S \tag{2.46a}$$

$$\frac{\partial I_P}{\partial z} = -\frac{\omega_P}{\omega_S} g_R I_P I_S - \alpha_P I_P \tag{2.46b}$$

where α_P and α_S are the fiber loss coefficients for pump and Stokes frequencies (ω_P and ω_S), respectively. Additionally, the coefficient $\frac{\omega_P}{\omega_S} > 1$ indicates that the energy supplied by the pump beam is more than the energy gained by the Stokes. Rest of the energy is lost in the system as heat via collisions.

The above differential equations do not have any analytical solution. However, for the small signal case ($I_S \ll I_P$), the pump depletion due to the amplification process can be neglected (first term in Eq. (2.46b)) and hence the solution becomes:

$$I_P(z = L) = I_0 \exp(-\alpha_P L) \tag{2.47a}$$

$$I_S(z = L) = I_S(0) \exp(g_R I_0 L_{eff} - \alpha_S L) \tag{2.47b}$$

where I_0 is the incident pump intensity, L is the propagation length and $L_{eff} = \frac{1-\exp(-\alpha L)}{\alpha}$

is the effective length. The gain term should be greater than the loss term in order to build up Stokes wave inside the fiber. This solution can only be applied for the initial stages of Raman amplification, because the small signal approximation will not be valid for so long due to pump depletion while amplifying Stokes.

2.5 Discrete vs. Distributed Amplifications

In optics, two different amplifiers, discrete and distributed, named by the gain medium placement, are used to compensate system losses. In discrete case, the lumped amplifiers are placed at discrete positions, i.e. once in 40-60 km for modern fiber-optic communication systems. On the other hand, in distributed amplification, the entire fiber optic cable link used to propagate signal, is utilized as a gain medium with co-propagating and counter-propagating pumping schemes. Stimulated Raman Scattering that is examined in the previous section governs the distributed amplification process.

2.5.1 Discrete Amplification

The optical amplifiers used in discrete amplification are generally bulky optical devices, which require specially doped fibers to achieve desired gain profile. Erbium Doped Fiber Amplifier (EDFA) is the most commonly used discrete amplifier where the core of a silica fiber is doped with Erbium ions. In order to attain gain in communication wavelength (1550 nm), it needs to be efficiently pumped with a laser at a wavelength of 980 nm or 1450 nm [25]. EDFA has a narrowband gain curve and the pump wavelengths are determined by the resonant energy levels of Er atom, as shown in Fig. 2.12. Additionally, EDFA has a slow gain process because of the energy storage at the upper level of Er atom.

2.5.2 Distributed Amplification

A flat gain Raman amplifier, based on stimulated Raman scattering, needs to be designed to provide a uniform amplification for the broadband signal. As mentioned earlier, the fiber becomes the gain medium for the Raman amplification when properly pumped that

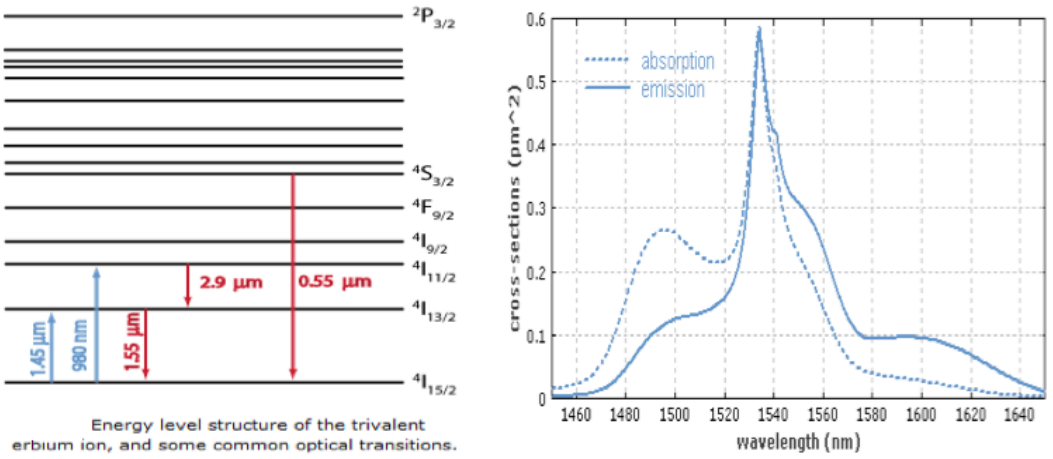

FIGURE 2.12: Energy level structure of Erbium ion and some optical transitions (a). Absorption and emission cross-sections for Erbium ions in Er: Yb-doped phosphate glass (b) [25].

causes pump depletion due to long fiber lengths [13]. In order to have more uniform amplification along the fiber, bidirectional (hybrid) pumping schemes consist of co-pumping (signal direction) and counter-pumping (opposite direction) may be facilitated, as shown in Fig. 2.13.

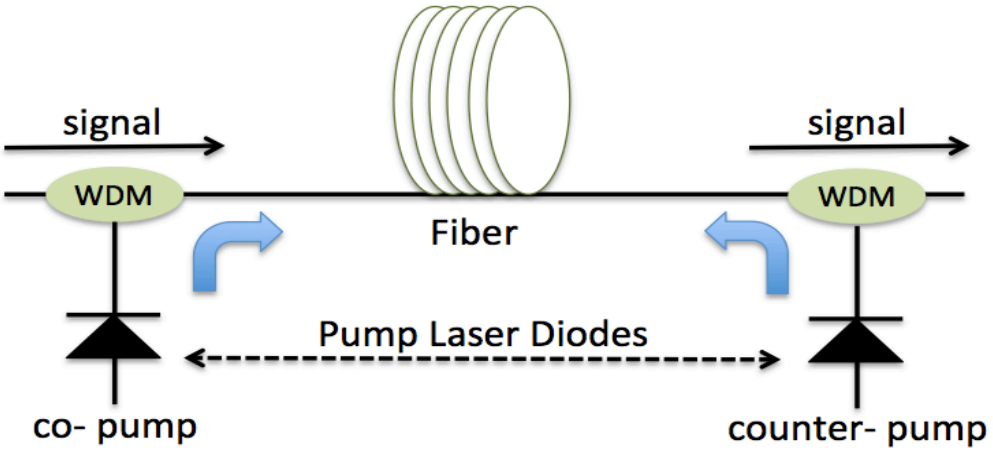

FIGURE 2.13: The schematics of the Raman amplifier including co/counter pump laser diodes [16].

The distributed Raman amplification becomes a great alternative to discrete amplification in terms of feasibility, achievable gain bandwidth, uniformity and the signal-to-noise ratio (SNR). The main advantages are as follow:

1. Raman amplification enables fast gain mechanism, since it employs a simultaneous process, SRS [13].

2. Raman amplification keeps the signal level inside the safe region through gain distribution over a long distance. In other words, it prevents the signals to reach high power levels where nonlinear effects are powerful and to drop below the noise floor where noise interference is drastic [26]. Kalyoncu et al. states that distributed amplification provides up to 16dB higher SNR corresponding to 2.5 bit higher resolution in TS-ADC setup [27].

3. Broadband and uniform spectral gain profile can be acquired with using multi pumping schemes and selecting appropriate pump wavelengths and the powers.

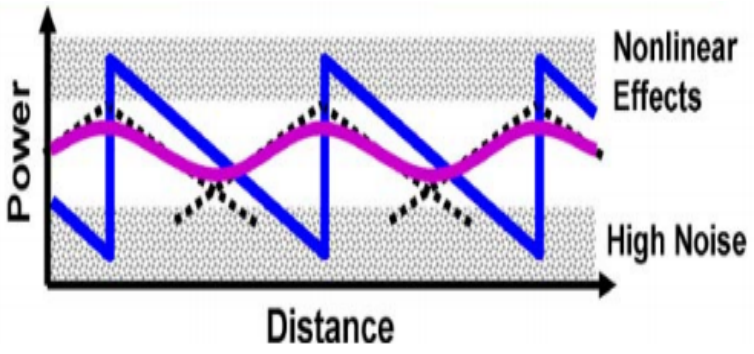

FIGURE 2.14: The signal level dynamics inside the fiber with discrete (blue) and distributed amplification (red) [26].

The multi-pumped Raman amplifier is modeled by including all signal-to-signal (pump-pump, pump-signal and signal-signal) interactions and the wavelength dependent attenuation (α_k). The following set of equations determines the evolution of all signal and pump powers along the Raman amplified system [16].

$$\pm \frac{dP_k}{dz} = -\alpha_k P_k + \sum_{j=1}^{k-1} g_{\lambda_j}(\lambda_k - \lambda_j) P_j P_k - \sum_{j=k+1}^{N} \frac{\lambda_j}{\lambda_k} g_{\lambda_k}(\lambda_j - \lambda_k) P_j P_k \tag{2.48}$$

where $k = 1, 2, \ldots, N$, +/- corresponds to co/counter propagating signals, P_k is the pump/signal power, α_k is the wavelength dependent attenuation coefficient and g_{λ_j} is the Raman gain coefficient for the signal at wavelength λ_j which is proportional to reference gain coefficient at λ_0 as $g_{\lambda_j}(\Delta\lambda) = \frac{\lambda_j}{\lambda_0} g_{\lambda_0}(\Delta\lambda)$. The first term on the right side of the equation represents the wavelength dependent fiber attenuation. The second term is the gain introduced on the signal at wavelength λ_k by the other signals with higher frequencies, $\lambda_j, j = 1, \ldots, k-1$. The last term, on the other hand, represents the pump depletion on the signal at wavelength λ_k due to power transfer to the other signals with lower frequencies, $\lambda_j, j = k+1, \ldots, N$ [16].

The set of equations above cannot be solved analytically, therefore numerical approaches such as generic and shooting algorithms, are generally used to calculate the proper pump wavelengths and powers to obtain desired uniform wideband gain profile. The Raman Amplifier used in our lab was designed by a senior student [16] using four pumps at 1450nm, 1470nm (forward), 1490nm and 1505nm (backward) in a hybrid pumping setup. Fig. 2.15 shows the gain profile of the designed Raman Amplifier.

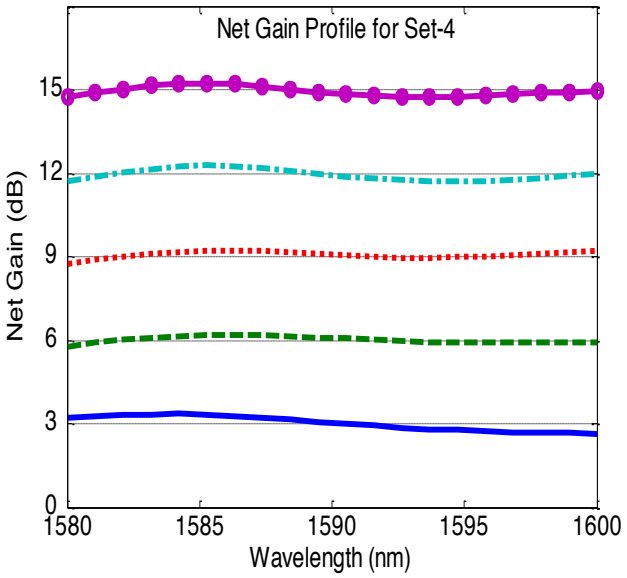

FIGURE 2.15: The optimized net gain profile of Raman amplifier over 1580nm to 1600nm [16].

Chapter 3

Photonic Time Stretch Systems and Time Stretch Analog to Digital Converter

The time-stretch ADC is the first application of photonic time stretching that employs the GVD in fibers. This chapter provides detailed explanation on the photonic time-stretch systems with more focus on TS-ADC. Additionally, the TS-ADC system is investigated both with simulations and experimentally. Also the effect of slowing down RF signals with the help of fiber dispersion is observed.

3.1 Introduction

The idea of stretching electrical signals goes back to the mid 20^{th} century. The all-electrical technique is utilized to match the data rates of signals to receivers when both have fixed frequency characteristics via using three dispersive networks and a mixer. This technique can provide signal slowdown and speedup, or time reversal [1]. At the end of the century, the optical time stretch system is realized experimentally with more focus on the signal slowdown because of the speed difference between optical and electrical systems [5, 6].

The rapid progress in CMOS technology with the availability of parallel computing increased the digital signal processor (DSP) speeds around few hundred GHz levels. However, ADC could not keep pace with them, thus becomes the key bottleneck in high-performance communication systems. Therefore, the amplified photonic time-stretch technique can be used to effectively slow down the electrical signal modulated on an optical envelope to the levels (1 GSa/s) that can be captured in real-time with a commercially available ADC. In addition to TS-ADC, it has enabled many applications from broadband communications to radar systems and real-time imaging that requires high-speed, high temporal or spatial resolution, and high throughput efficiency [28]. On the other hand, it facilitates capturing of ultrafast rare events in real-time that is highly desired in wideband ADC [26, 29], spectroscopy [30] and imaging [31].

In optical domain, dispersion can be achieved by several dispersive elements such as optical fibers, chirped fiber Bragg gratings, prisms. However, their usage depends on the operating wavelength. For example, the dispersion ability of single mode fiber cable is really good at the wavelengths around 1550nm, but not in visible spectrum. Therefore, the groups who employ the visible lasers facilitate other techniques such as prisms to create a frequency dependent delay [4].

3.2 Experimental Setup

Photonic time stretched systems mainly consist of the broadband illumination, spectral domain processing and time to wavelength mapping modules, as illustrated in Fig. 3.1. The supercontinuum generation is achieved by propagating the Mode Locked Laser (MLL) pulses through the amplifier (EDFA) and the supercontinuum (SC) fibers [32]. The generated broadband window is filtered by coarse wavelength-division multiplexing (CWDM) to obtain ~20nm flat region. The generated broadband spectrum is either mapped over the time via dispersion compensation module (DCM) or space via diffractive elements. Then, the wavelengths are shaped by the information of interest, which can be a fast arbitrary electrical signal, the spectroscopic signature of a materials or the image of an object. Finally, the modulated spectrum is converted into time domain via time stretching. In other words, spectrally modulated SC pulses are propagated through the highly dispersive fibers to perform Dispersive Fourier transformation, which transforms the frequency domain into temporal domain. In imaging setup, the time, wavelength,

and space mappings are achieved through diffraction grating and DCM. Therefore, the order of mapping can be changed in order to eliminate the coupling losses from free space into the fiber.

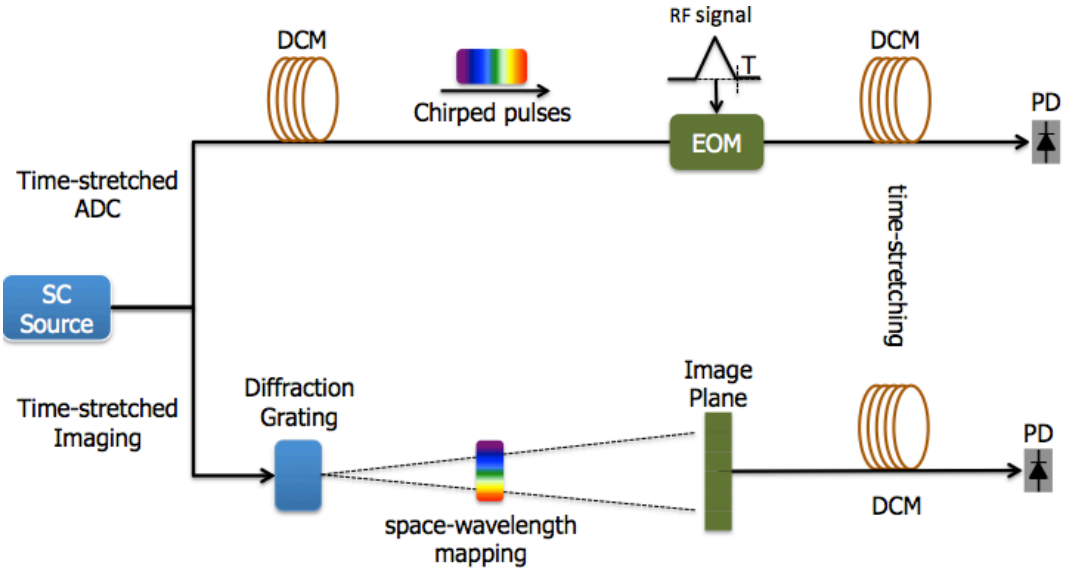

FIGURE 3.1: The schematic of the photonic time-stretched analog-to-digital converter and imaging systems [16].

In order to effectively enable time-wavelength mapping, the temporal resolution of the system, which is the temporal width ($\Delta\tau$) of the SC pulses, has to be short enough to catch the high frequency features. In other words, the optical bandwidth has to be much higher than the electrical bandwidth to effectively sample the RF signal without any loss due to well-known Nyquist theorem as $\Delta\tau \ll \Delta T = 1/(2\Delta f_{RF})$ yields to $2\pi\Delta f_{opt} \gg \Delta f_{RF}$ [29]. Since the optical bandwidth is typically in the THz range whereas the RF bandwidth is in GHz range, the condition for time-to-wavelength mapping is normally satisfied. As discussed in Chapter 2, nonlinear dispersion as characterized by the higher order dispersion terms $(\beta_3, \beta_4, \ldots)$ causes different spectral segments to stretch in different amounts in a nonlinear manner so that the time stretching becomes time dependent. The group delay ($\Delta\tau$) for a certain bandwidth ($\Delta\lambda$) per unit length of the fiber is calculated as $\Delta\tau = \int_{\Delta\lambda} D(\hat{\lambda})d\hat{\lambda}$. At the output, the temporal width of the SC pulses becomes $\Delta t_{out} = L\Delta\tau$ [16].

The peak intensity is degraded due to system loss and broadening effect. Optical amplification should be employed, especially over the second DCM which has a longer length $L_2 = (M-1)L_1$, in order to achieve high stretch factors (M). Optical amplification can

be utilized either by embedding EDFA at discrete positions or by distributing the gain over the system as in Raman amplifier [29].

The spectrally modulated pulses are stretched along the 2^{nd} DCM. After that, modulated optical pulses are converted to electrical domain via single photodetector and observed by an oscilloscope. In TS-ADC system, photodetector and oscilloscope provides the analog-to-digital conversion together.

3.2.1 Supercontinuum Generation

In time stretch systems, the broadband source is required, since the width of time window that will host the RF signal, will be determined by the spectral width of initial optical pulse through equation $\Delta t \simeq D \cdot \Delta\lambda$. The broadband spectrum is created by nonlinear interactions in fibers, therefore MLL pulses are amplified by an EDFA to increase the effect of SPM. Finally, CWDM is used to carve out ~20nm bandwidth around 1590nm from the generated broadband (~150nm) spectrum. The experimental setup and pulse evolution in fibers are illustrated in Fig. 3.2. As it is seen in the figure, SMF fiber does not change the spectrum so much, but some deformations occurred at the center of the pulse due to high intensity. The other two fibers are generally expanded the spectrum with small distortions and peak/valley formations at the center.

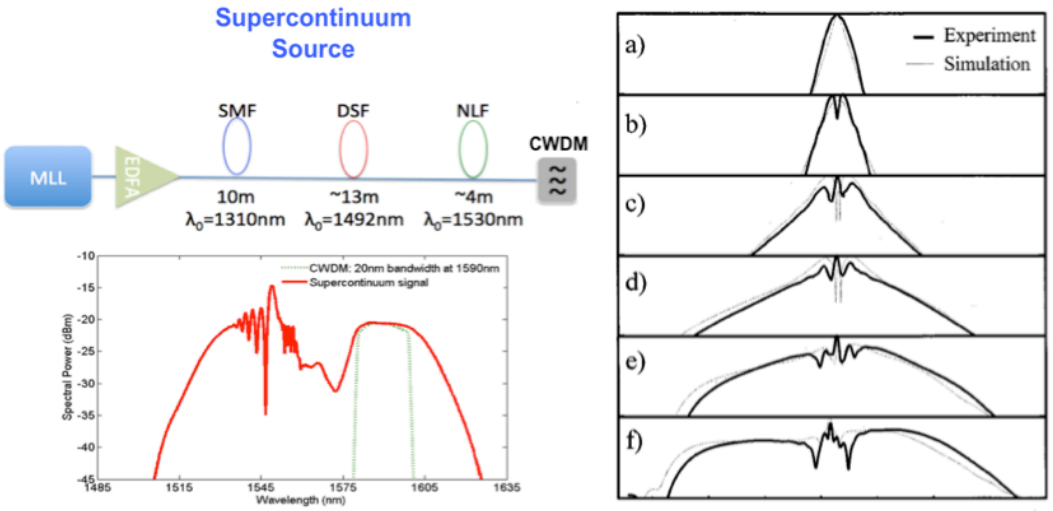

FIGURE 3.2: The experimental setup to generate SC pulses and generated spectrum before/after CWDM filter (left) [8] and spectral evolution of SC pulses inside fibers at 0m (EDFA output), 10m, 23m, 24.5m, 26m, 27.5m respectively (right) [32].

3.2.2 Dispersion Compensated Modules

Dispersion Compensated Modules are just a spool of fibers that have named according to the total dispersion D in terms of (ps/nm). They disperse the pulses based on the GVD. In TS-ADC, the first module is giving chirp to the optical pulses with creating time window $\Delta t \simeq D_1 \cdot \Delta\lambda$. On the other hand, second is used to create desired stretch factors $M = 1 + L_2/L_1$. The second module is generally amplified with distributed amplification. In our setup, we employed four laser diodes at 1450nm, 1470nm, 1490nm, and 1505nm to pump DCM from both sides as shown in Fig. 3.3. The pump lasers are continuous wave lasers that transfer some of their energy to the pulsed signal while propagating along the fiber (2^{nd} DCM) through the SRS process. In order to achieve flat gain spectrum, four different laser diodes are employed in the setup.

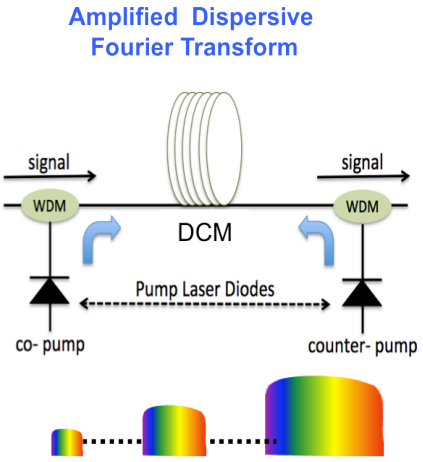

FIGURE 3.3: The schematic of Amplified Dispersive Fourier Transform.

3.2.3 Mach-Zehnder Interferometer

Electro-optic modulators (EOM) are used to modulate optical pulses according to a reference electrical signal. Mach-Zehnder (MZ) Interferometric design has two branches where at least one branch employs Lithium Niobate ($LiNbO_3$) based modulator to create a phase delay. The amount of phase shift creates constructive and destructive interferences in order to modulate the optical intensity. Some MZ interferometers create two outputs where the envelope is also propagated besides the modulated signal that eases the extraction of RF signal from the envelope.

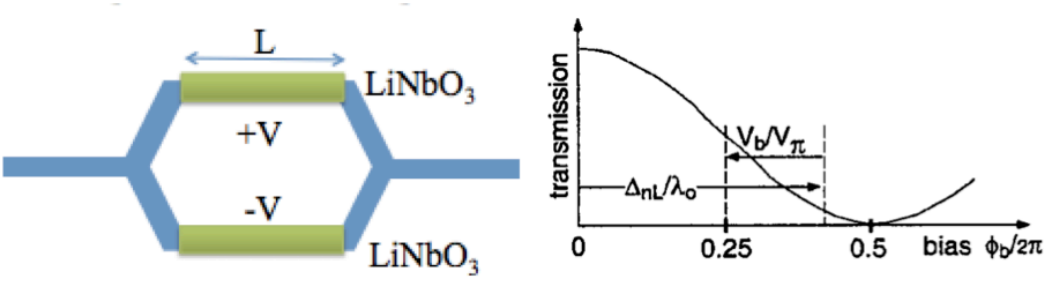

FIGURE 3.4: The schematic of MZI [12] and transmission function of WIB [33].

Figure 3.4 illustrates the schematic of MZI and the sinusoidal transmission function which is formulated as [33, 34]:

$$T(\lambda) = \frac{1}{2}\left[1 + \cos\left(\pi \frac{V}{V_\pi(\lambda)} + \phi_B(\lambda)\right)\right] \tag{3.1}$$

where $\phi_B = \phi_\Delta + \phi_V$ is the phase bias of the modulator and

$$\phi_\Delta = 2\pi \frac{\Delta_{nL}}{\lambda} \tag{3.2a}$$

$$\phi_V = \pi \frac{V_B}{V_\pi} \tag{3.2b}$$

where Δ_{nL} is the internal path length mismatch between two arms of the MZ interferometer and V_B is applied bias voltage.

In order to suppress the second-order distortion, the bias point must be independent of the wavelength meaning that

$$\frac{d\phi_B}{d\lambda} = \frac{d\phi_\Delta}{d\lambda} + \frac{d\phi_V}{d\lambda} = 0 \tag{3.3}$$

The derivatives will be calculated with substituting phase terms with Eq. (3.2), resulting that [34]

$$\frac{d\phi_\Delta}{d\lambda} = -\frac{1}{\lambda}\phi_\Delta \tag{3.4a}$$

$$\frac{d\phi_V}{d\lambda} = -\frac{1}{V_\pi}\frac{dV_\pi}{d\lambda}\phi_V \tag{3.4b}$$

$$\frac{1}{\lambda}\phi_\Delta + \frac{1}{V_\pi}\frac{dV_\pi}{d\lambda}\phi_V = 0 \tag{3.4c}$$

In order to operate Mach-Zehnder Modulator in the linear region, the following conditions should apply.

i) $\phi_B = \pi/2$ at λ_0

ii) $d\phi_B/d\lambda = 0$ at λ_0

V_π is one of the fundamental parameters for MZ modulators, which has a complex formula to calculate [33]. Therefore, we directly used the values given in the datasheets and chose the bias voltage with assumption that the two arms are exactly matched ($\phi_\Delta = 0 \rightarrow \phi_B = \pi V_B/V_\pi \rightarrow V_B = V_\pi/2$). Later, the bias voltage can be tuned to get the midpoint exactly.

3.3 Mathematical Analysis of TS-ADC Systems

In order to analyze the TS-ADC system, an ultra-short transform limited Gaussian pulse is employed as an input optical pulse. The evolution of such pulses along the experimental setup will be mentioned step by step. Input pulse will be simple Gaussian as

$$E(z=0,t) = \exp\left(-\frac{t^2}{\tau^2}\right) \tag{3.5}$$

It will be chirped in the DCM module of length L_1 and will be

$$E(L_1,t) = \exp\left(-\frac{t^2}{\tau^2}\right)\exp\left(-\frac{jt^2}{2L_1\beta_2}\right) \tag{3.6}$$

where $L_1\beta_2 \ll \tau^2$, which physically means that there should be so high broadening effect ($T_1/T_0 \gg 1$). This condition is always satisfied for subpicosecond pulses after propagating several hundreds meters. The spectrum of the pulse can be represented as follow:

$$E(L_1,f) = \frac{\sqrt{\pi}}{\left|\sqrt{\tau^{-2}+\frac{j}{2L_1\beta_2}}\right|}\exp\left(-\frac{\pi^2 f^2}{\tau^{-2}+\frac{j}{2L_1\beta_2}}\right) \tag{3.7}$$

The chirped pulse is intensity modulated in the $LiNbO_3$ based MZ Interferometer with a sinusoidal signal at f_m. The modulation depth (α) inside the MZI is small enough to neglect higher order harmonics of modulation frequency f_m. Modulated electric field will be

$$E_m(L_1,f) = E(L_1,f) * \left[\delta(f) + \frac{\alpha}{2}\{\delta(f-f_m)+\delta(f+f_m)\}\right] \tag{3.8}$$

where " $*$ " denotes convolution. After 2^{nd} DCM module, the output spectrum will be

$$E_{out}(L_1+L_2,f) = E_m(L_1,f)\exp(j2\pi^2 L_2\beta_2 f^2) \tag{3.9}$$

When we substitute the closed form equations of the terms in Eq. (3.9), it will transform to

$$E_{out}(L_1+L_2,f) = \frac{\sqrt{\pi}}{\left|\sqrt{\tau^{-2}+\frac{j}{2L_1\beta_2}}\right|}\exp(j2\pi^2 L_2\beta_2 f^2) \left[\exp\left(-\frac{\pi^2 f^2}{\tau^{-2}+\frac{j}{2L_1\beta_2}}\right)+\frac{\alpha}{2}\left\{\exp\left(-\frac{\pi^2(f-f_m)^2}{\tau^{-2}+\frac{j}{2L_1\beta_2}}\right)+\exp\left(-\frac{\pi^2(f+f_m)^2}{\tau^{-2}+\frac{j}{2L_1\beta_2}}\right)\right\}\right] \tag{3.10}$$

The inverse Fourier transform of Eq. (3.10) will be [7]

$$E_{out}(L_1+L_2,t) = \sqrt{\frac{L_1}{L_1+L_2}}\exp\left(-\frac{t^2}{\tau^2(\frac{L_1+L_2}{L_1})^2}\right)\exp\left(-\frac{jt^2}{2(L_1+L_2)\beta_2}\right) \times\left[1+\frac{\alpha}{2}\cos\left(2\pi f_m t\frac{L_1}{L_1+L_2}\right)\right]\exp\left(j2\pi^2 L_2\beta_2 f_m^2\frac{L_1}{L_1+L_2}\right) \tag{3.11}$$

The output electric field will go to the detector and convert to the intensity as follow:

$$I_{out}(L_1+L_2,t)\propto E_{out}(L_1+L_2,t)E^*_{out}(L_1+L_2,t) = \frac{L_1}{L_1+L_2}\exp\left(-\frac{2t^2}{\tau^2(\frac{L_1+L_2}{L_1})^2}\right) \times\left[1+2\alpha\cos\left(2\pi f_m t\frac{L_1}{L_1+L_2}\right)\cos\left(2\pi^2 L_2\beta_2 f_m^2\frac{L_1}{L_1+L_2}\right)\right] \tag{3.12}$$

The output intensity indicates that the pulse is stretched by $M = 1 + L_2/L_1$, since the peak intensity is scaled down by M, so the Gaussian envelope and modulation frequency f_m as seen in Eq. (3.12). The last term represents the dispersion penalty that limits the maximum frequency of the system and the transfer function is its square such as [7]

$$H_{att} = \cos^2\left(2\pi^2\beta_2\frac{L_2}{M}f_m^2\right) \tag{3.13}$$

Figure 3.5 shows the calculated transfer function for M=45, L_1=1km, so L_2=44km.

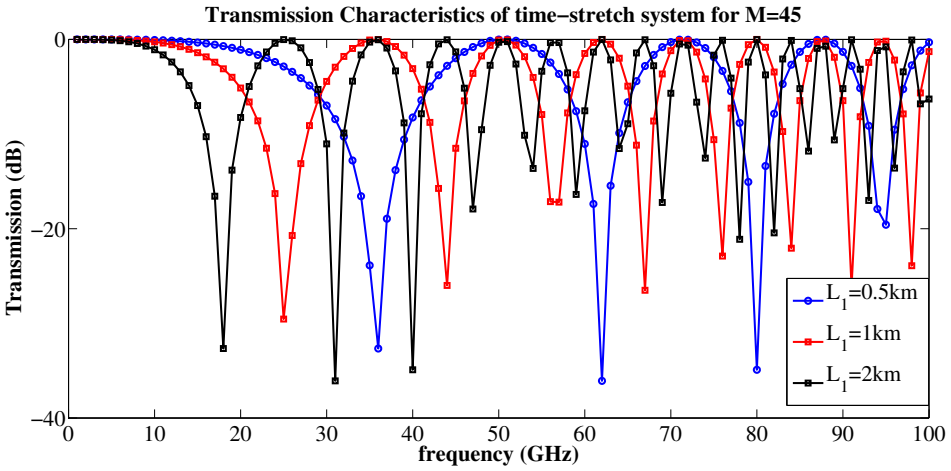

FIGURE 3.5: The transfer function of TS system with M=45.

3.4 Results

3.4.1 Simulation Results

In simulations, the ultra-short ($T_{FWHM} = 250fs$) transform limited (C=0) Gaussian pulses are used instead of SC source. The Gaussian Pulses are linearly chirped while propagating through the initial fiber spool, which has length ($L_1 = 1km$) and dispersion (D=100ps/nm-km), thus ~1.4ns time window is formed. After that, the pulse intensities are modulated according to 36GHz sinusoidal RF signal, since the transfer curve (red plot in Fig. 3.5) has a peak at this modulation frequency for the stretch factor M=45. The modulated optical pulses went through another DCM module including 44 km fiber, and stretched together with the RF signal. Therefore, the modulation frequency is scaled down to 800MHz. The figures from Fig. 3.6 to 3.9 illustrate the evolution of pulses along the TS-ADC system.

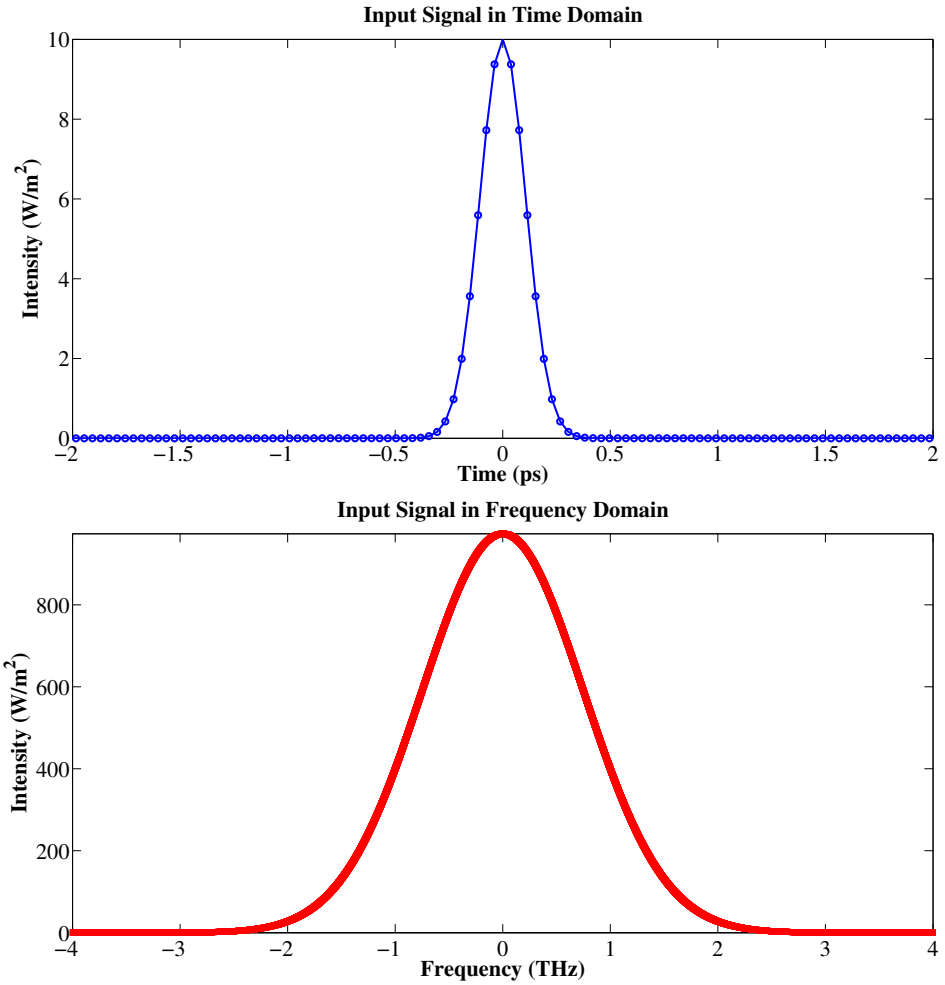

FIGURE 3.6: The input Gaussian pulse in time and frequency domain.

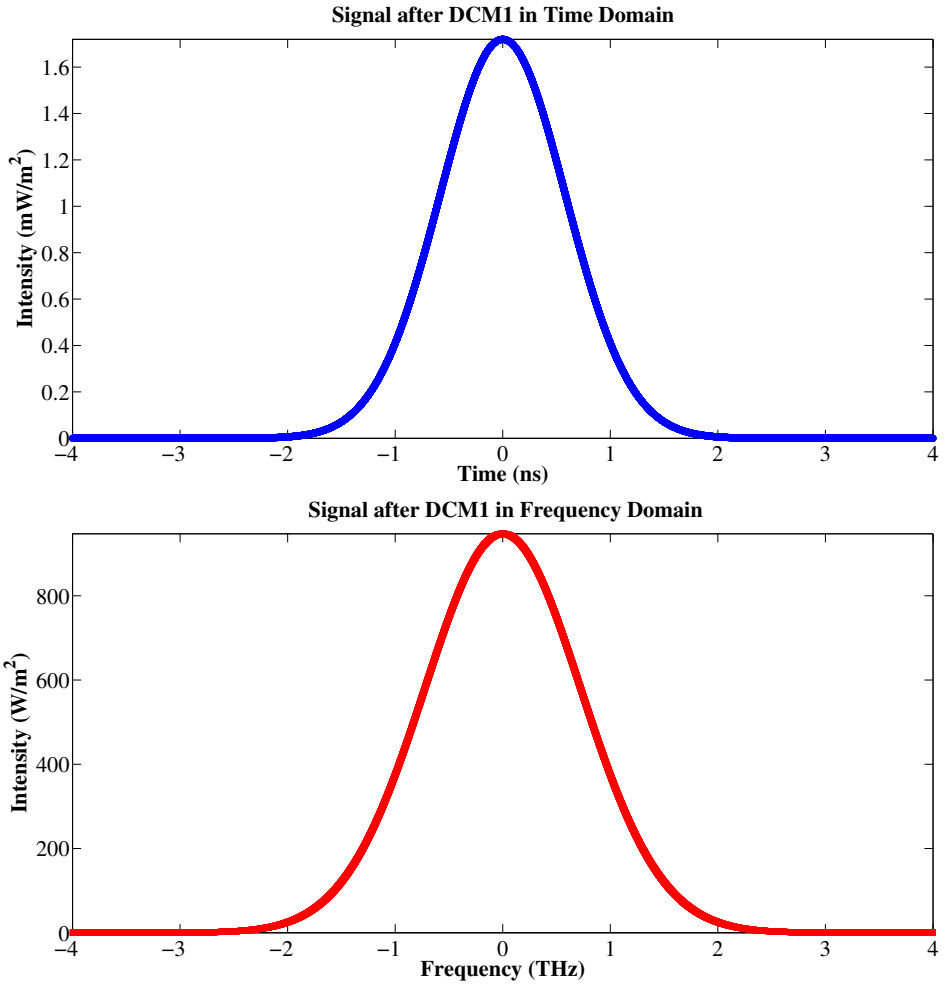

FIGURE 3.7: Evolution of the signal at the output of first DCM (L=1km) in time and frequency domain.

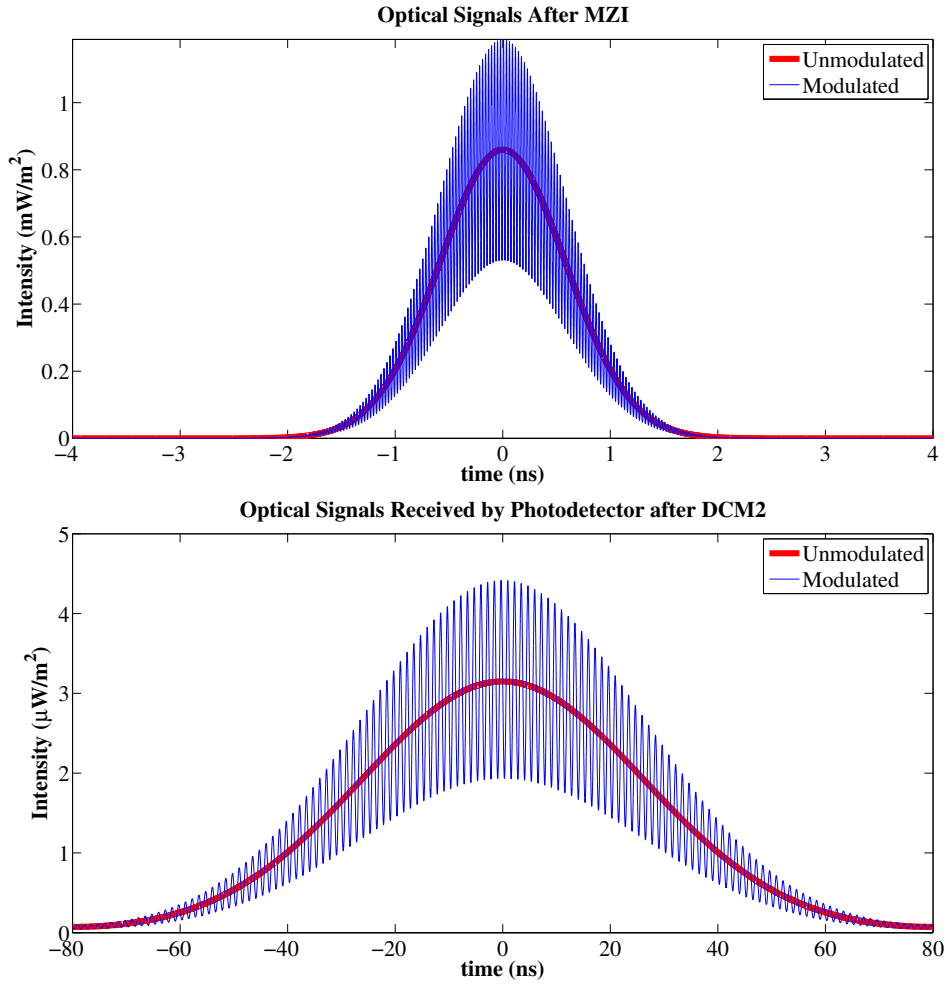

FIGURE 3.8: Intensity modulated optical pulse after the MZ Interferometer (up) and after the second DCM and detection (down).

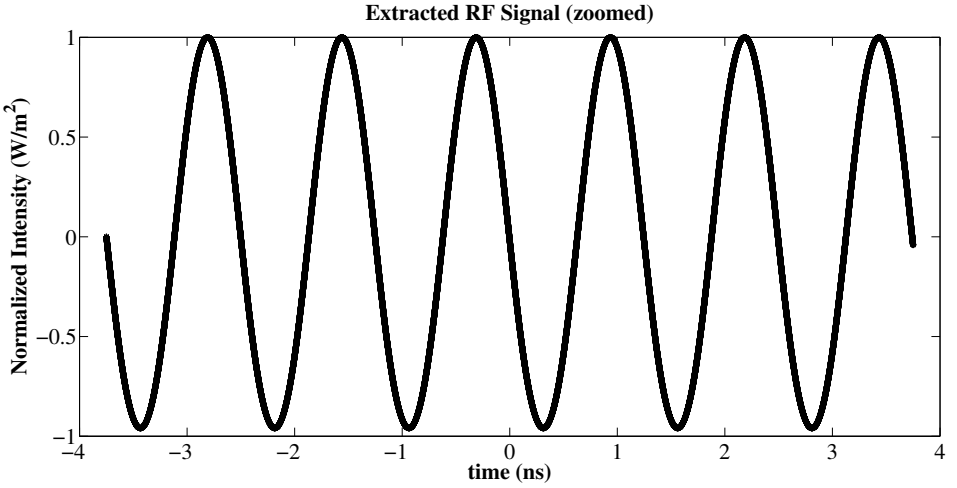

FIGURE 3.9: Extracted RF Signal at 800MHz due to 45 times stretching.

3.4.2 Experimental Results

In the experimental setup, we used the broadband SC source with ~20nm bandwidth centered at 1590nm. The pulses are propagated through a DCM with D=-40 ps/nm that creates 800ps initial time window. After that the optical signal is modulated inside a $LiNbO_3$ based EOM according to the sinusoidal RF signal generated by tunable Yttrium iron garnet (YIG) oscillator operating at 8GHz. The RF signal is combined with DC bias through a bias tee, since the EOM used in the experiment has only one electrical input port. The modulated optical pulses propagated through the second DCM that is amplified by a Raman amplifier utilizing 4 laser diodes (1450nm, 1470nm, 1490nm and 1505nm) in bidirectional pumping mechanism to attain wideband flat gain over the desired spectrum and along the fiber spool. The second DCM has a total dispersion of -658 ps/nm provided by 8km special fibers with 0.34dB/km propagation loss and 0.45dB splice loss [16]. Therefore, the system has a stretch factor of $(40+658)/40 = 17.45$, thus the modulation frequency will scale down to $8GHz/17.45 = 458.45MHz$.

Figure 3.10 shows the detected time stretched optical wave carrying RF signal. The Gaussian filters shown in Fig. 3.11 are designed to eliminate the noise and catch the envelope by utilizing the high and low frequency characteristics of noise and envelope, respectively. As a result, the extracted RF signal, shown in Fig. 3.13, is a bit off with 3.87% error from the calculated value which may be caused by the distortions, mismatches between DCM modules, imprecise oscillation frequency of YIG oscillator, etc.

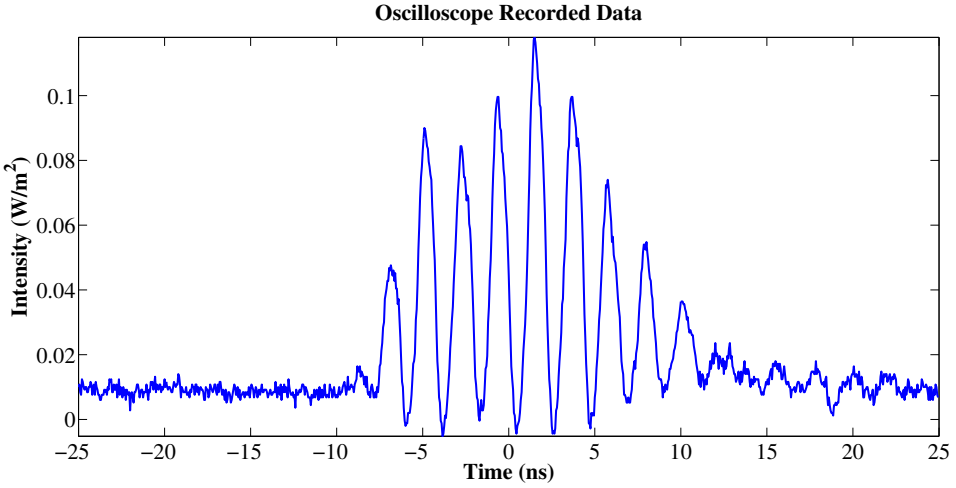

FIGURE 3.10: Detected wave on the oscilloscope.

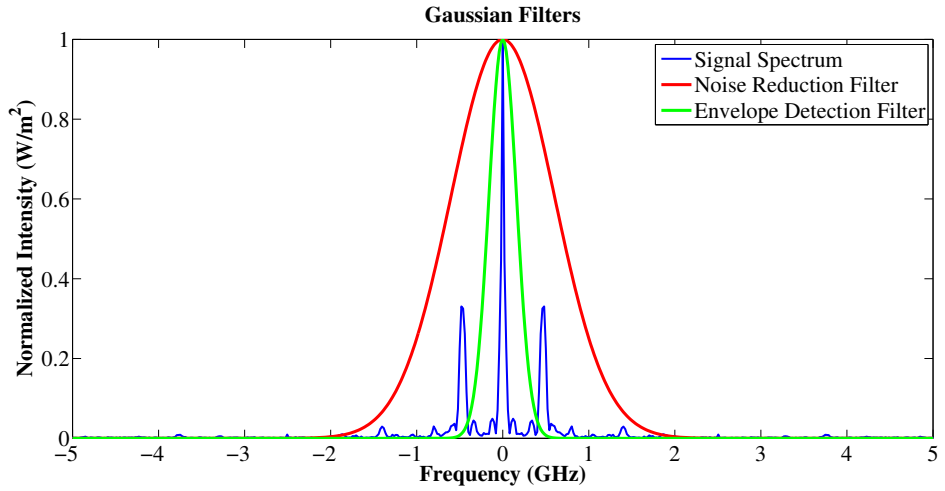

FIGURE 3.11: Spectrum of the detected wave and the designed Gaussian filters.

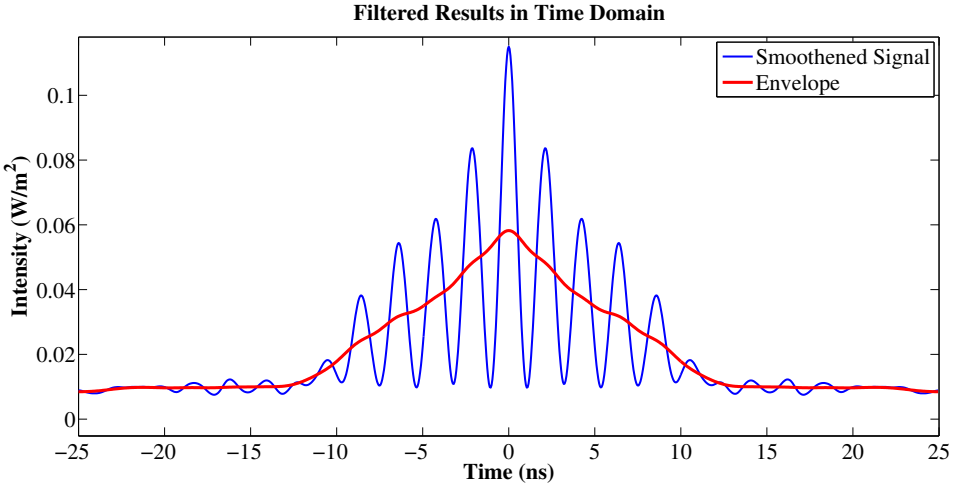

FIGURE 3.12: Smoothened Signal and Envelope after Gaussian filters.

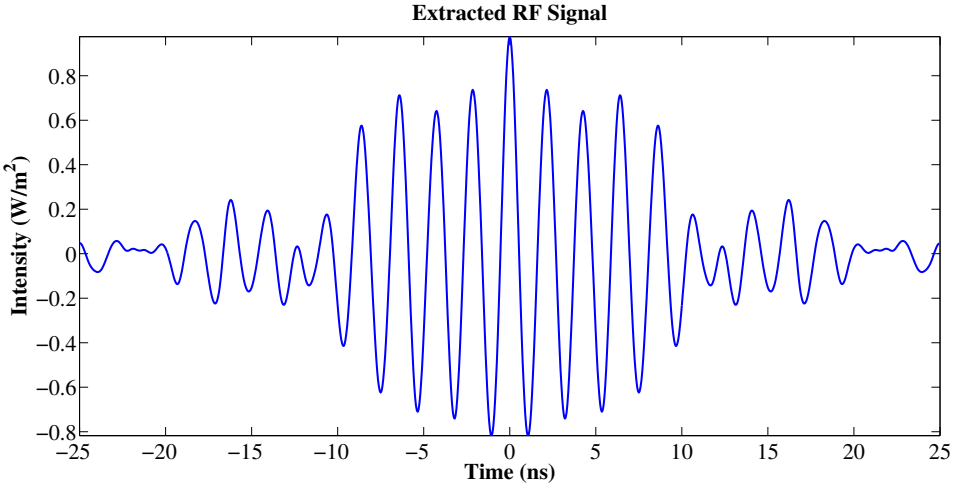

FIGURE 3.13: Extracted sinusoidal RF signal with 2.1ns period, namely ~476.2MHz.

3.5 Conclusion

In this chapter, amplified time stretched system, which is employed in real time applications such as optical analog-to-digital converter, arbitrary waveform generation and dispersive imaging, is investigated. The simulations are done to understand the behavior of individual components used in the TS-ADC. The TS-ADC facilitates the basic components such as dispersive components, modulators, receiver etc. that are also employed in several other applications from communication to imaging. Therefore, it was a good introductory section for those new to the optics field.

Chapter 4

Scalable Fast Dispersive Laser Scanner by Using Digital Micro Mirror Arrays

The idea of time-stretching is applied to other fields such as Optical Arbitrary Waveform Generation and Real-Time Imaging after the TS-ADC with facilitating other free-space optical components. In this chapter, a novel real-time imaging system designed for surface metrology in micro manufacturing is presented. The system employs time-stretching, DMDs and diffraction grating to achieve time, wavelength and space mapping to image the 2D target.

4.1 Introduction

With the advent of micro manufacturing technology, extremely fine surface engineered solids are now reality for higher performance or for new functionalities. For instance, hydrogen fuel cells utilize bi-polar plates with microfluidic channels of dimensions as small as 5μm at the surface to convert fuel into power via electrochemical conversion [35]. In the near future, hydrogen fuel cells are expected to become one of the main alternative energy sources and hence there will be demand for mass production of plates with micro fluidic channels, especially for automotive industry [36]. However, as the mass

manufacturing of these micro textured solids becomes reality, the rapid quality control becomes a fundamental bottleneck for high yield.

Characterization of surface texture is an interest of surface metrology and it has been investigated extensively. Up to date several techniques have been developed, mostly specialized on one aspect of the measurement at a time such as measurement of the overall shape, the small-scale features, waviness and the roughness of the surfaces [37]. In general these various surface metrology methods are classified under three categories such as the stylus instruments, scanning probe microscopy, and optical scanning techniques. The first technique, which is based on drawing stylus tip over the surface at constant speed, can enable up to several millimeters wide area with the detection of fine details down to $\sim 1\mu$m [38]. The second technique, which relies on very low contact forces between tip and surface, provides relatively highest lateral resolution ($\sim$1nm) and vertical resolution down to sub nanometers, but lacks of scanning speed and limited to small scanning areas [39]. Optical scanning techniques, on the other hand, measure the surface topography by illuminating the surface through optical system and processing the reflected or transmitted light without destructive physical contact. Among these, interferometric microscopes [40] based on phase shifted interference enable monitoring of wide area with high vertical resolution ($<$0.1nm) and lateral resolution close to $\sim 0.1\mu$m. Alternatively, confocal microscopy [41], namely a focused beam version of stylus, achieves higher lateral resolution by use of a pinhole, and it is very widely used technique. Higher resolution is achievable by any of these techniques at the expense of scanning area and speed.

Fast laser scanning technology is highly desired in many applications ranging from defense to sensing and micro-manufacturing to increase the imaging speeds [42–44]. Especially, high speed ($>$1kHz) scanning is essential for multi-dimensional monitoring of moving objects and to capture fast transient information of a dynamic process pertinent to light detection and ranging (LIDAR) [45, 46], structural dynamics [47, 48], surface vibrometry [49], observation of biomechanical motility [50], cellular network dynamics [51], confocal and multi-photon microscopy [52, 53] applications. In addition, scanning of wide area or many objects in a short period of time is also important for such high-throughput applications as atmospheric science [45], endoscopy and cytometry for medical diagnosis [54, 55], geographical survey and surface profilometry in the semiconductor industry, and surface characterization and quality control in micro-manufacturing [42–44]. Various types of laser scanning techniques enabling higher scan rates have been recently proposed.

Galvanometric mirrors known as the mechanically scanning mirrors are widely used for beam steering. The scanning speed of such high inertia mirrors is limited to ~10kHz in 1D and ~100Hz in 2D [56]. Alternatively, frequency-tunable laser in a diffractive optic bench has recently been demonstrated to achieve more than 10 times higher scanning rates [57]. In addition to the methods mentioned above, new all-optical techniques using acousto-optic deflectors (AOD) are used as a tunable diffraction grating to deflect the beam via electronically changing the angle of 1^{st} diffraction order. Millimeter scale area imaging with $<10\mu$s scanning speed and few micrometer scanning resolution has been achieved [58]. Well known real time dispersive imaging system providing ultra fast frame rates up to tens of MHz combined with a beam deflector to enable 2D wide area scanning has been recently demonstrated [4]. However, AOD is deficient in terms of power transfer efficiency and limited deflection angles, and hence scanning area.

The goal of this project is to demonstrate fast dispersive laser scanning system. Here we achieve ~20mm^2 wide area scanning with ~150μm lateral and ~160μm vertical resolution at 5kHz scanning rate by using DMD technology. DMDs provide alternative fast area scanning technology that can achieve dynamic sectioning of modulated patterns via pixelated MEMS mirrors. Our proposed method using DMD technology can provide fast scanning rates up to 32.5kHz (~1000 times faster than conventional scanners) and resolution down to single mirror pitch size of 10.8μm with the state of art MEMS technology.

The DMD technology is preferred for real time imaging, because it provides high resolution, high reflection, exceptional stability and excellent controllability over thousands of individual micro mirrors. Also, it has already been commercialized for many applications ranging from confocal microscopy, optical networking, 3D metrology, spectroscopy to medical applications [59–61]. By spatially switching the light through micro-mirror arrays, DMD can be utilized as a digital reflective spatial light modulator (SLM). In comparison to most commonly used liquid crystal display (LCD) technology, such devices provide extremely high 2D scanning speeds up to 32.5kHz ($<30\mu$s fast switching speed), higher fill factor of 90% than the liquid crystal with 70%, ~6.6 times higher power transfer efficiency, ~11 times higher contrast ratio, as twice as higher diffraction efficiency of 88% and feasibility for wide range of wavelengths (UV to NIR) [62, 63].

4.2 Digital Micro-mirror Device

DMD is a pixelated MEMS device created by Texas Instruments with using its extremely powerful and flexible DLP^{TM} technology. It has an array of individually addressable optoelectromechanical pixel units. Each pixel unit consists of aluminum micro-mirror, mechanical assembly and the control electronics, as illustrated in Fig. 4.1. The mechanical assembly includes metal-3 layer, torsion hinge and the yoke. A mirror post connects the micro-mirror to yoke, which is the base for the mirror. The yoke is rotatable over diagonally placed two torsion hinges due to the electrostatic attraction between mirror address electrode on the yoke and yoke address electrode on metal-3 layer. The metal-3 layer lands on the memory cell that consists of metal pads and mechanical stops to determine the maximum rotation angle. Control electronics include CMOS SRAM (complementary metal oxide semiconductor based static random-access memory) cell that keeps the state of the mirror set through a computer software as a binary data (1 or 0). After the CMOS SRAM is loaded with the binary data, the electrodes on the metal-3 layer are charged accordingly to produce electrostatic attraction of yoke and as well the mirror elements to rotate in the specific direction [64].

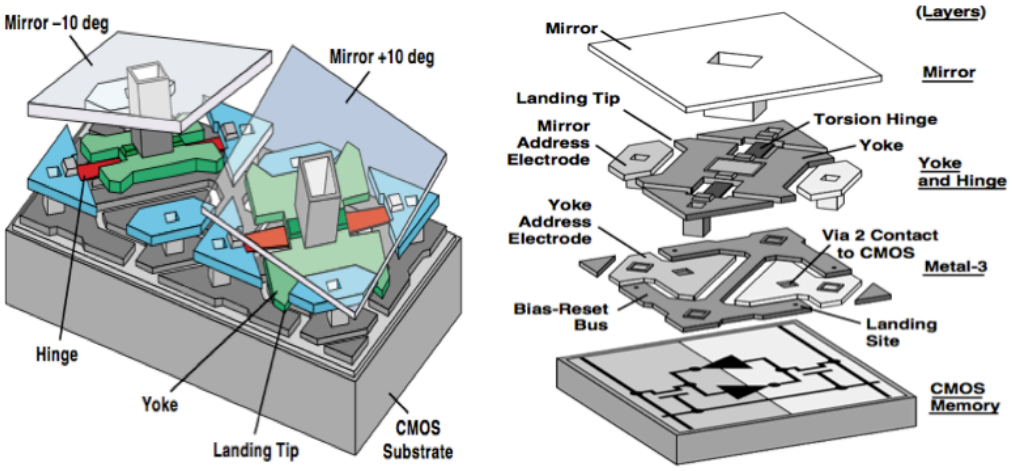

FIGURE 4.1: The mechanical and electrical control assemblies of the digital micro-mirror memory cell [64].

The maximum achievable frame rate is the fundamental performance parameter of the DMD controller board. The state of the art DMDs can achieve up to 32.5kHz frame rate. Other physical properties such as the array size, maximum tilt angle and the mirror pitch size are tabulated in Table 4.1 for the commercialized current DMD chipsets. As it is shown, while pitch size can go down to 7.56μm, the array size can reach to 1920x1080.

In our experimental setup, we have used 0.55XGA chipset with 10.8μm pitch size, 12^o tilt angle, and 1024x768 array size.

TABLE 4.1: The currently available DMD chipsets from Texas Instruments [65].

Chipset	Mirror Pitch size	Mirror Tilt angle	DMD Array size
0.17 HVGA	7.56μm	12^o	480x320
0.55 XGA	10.8μm	12^o	1024x768
0.3 WVGA	7.6μm	12^o	608x684
0.7 XGA	13.6μm	12^o	1024x768
0.95 1080p	10.8μm	12^o	1920x1080

4.2.1 DMD Operation

The incident light is reflected through specific directions via tilting the micro-mirrors by controlling the DMD. Each micro-mirror has three different states defined as the flat, ON and OFF. Flat is the default state (neutral position with 0^o tilt angle), when the DMD is switched off, otherwise it cannot be achieved. The other states (ON/OFF) can be achieved according to the loaded binary data into the CMOS SRAM cell. Also, DMD can switch the micro-mirrors between the ON-OFF (+/- $\theta_T = 12^o$) states according to the bit stream [66, 67]. As it is seen in Fig. 4.2, in ON/OFF states, the reflected light deviates +/- $2\theta_T$ degrees from the specular reflection due to the fundamental rule of reflection ($\theta_{inc} = \theta_{ref}$).

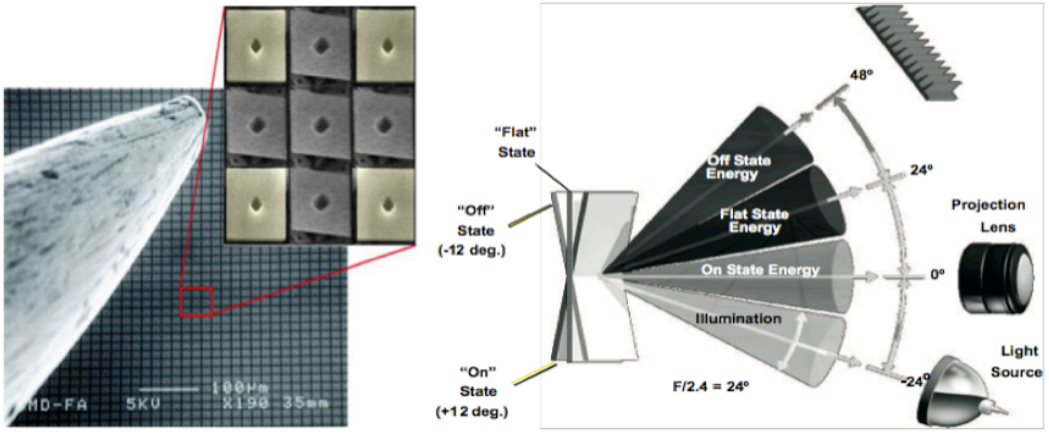

FIGURE 4.2: The microscopic view (a) of DMD and the micro-mirrors in two different states. The optical function (b) of 12^o micro-mirror tilt device [67].

DMD can be loaded with binary image patterns to create any desired illumination. The binary image patterns can easily be formed in MATLAB via creating 1024x768

matrices with ones and zeros. Gray scale intensities can also be achieved by dynamically switching mirrors with using pulse-width modulation (PWM), besides the black and white projection when the mirrors are statically assigned to a state. In PWM, the pattern is dynamically switched according to the binary code representation to increase or decrease the duty cycle, which will determine the gray scale intensities quantized between 0 and 1, as illustrated in the Fig 4.3. The N bit binary PWM system can be designed to obtain 2^N gray scale intensities where each i^{th} significant bit covers $\frac{2^{i-1}}{2^N-1}$ percentage of time [64, 68]. However, the DMD is used as a beam steering device in order to scan a wide area as line-by-line.

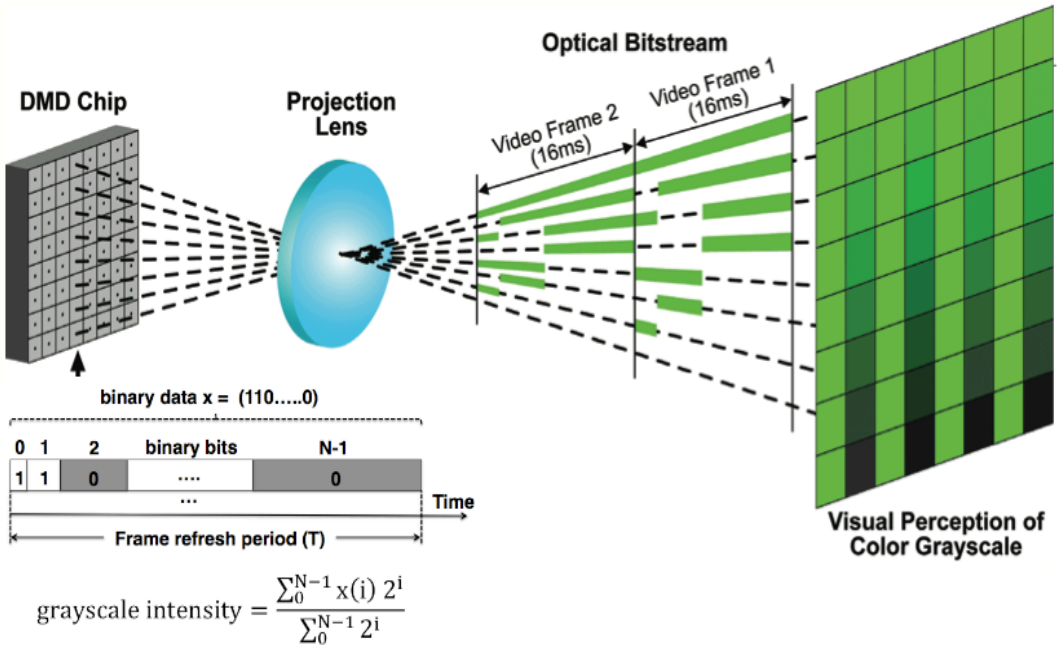

FIGURE 4.3: The binary N bit PWM system designed to obtain grayscale intensity levels [68].

4.2.2 DMD Properties: Advantages and Disadvantages

DMD is a micro-optical device designed to be used as a digital spatial light modulator by providing much better optical performance in terms of speed, feasibility for broadband illumination, active area, contrast ratio and the diffraction efficiency than the other types of SLMs [63]. The main advantages and the disadvantages of the DMD in comparison to most commonly used liquid crystal display (LCD) technology are listed below:

Advantages :

1. With the state-of-the-art MEMS micro-mirror technologies, up to 32.5 kHz pattern rate with a fast switching speed of less than 30μs between the states, allows fast display of illumination patterns. On the other hand, LC based SLMs can achieve at most the time scale of milliseconds.

2. The LC-SLM is a transmissive device, however the DMD is reflective. While the light is transmitting through the cascaded glass layers, it experiences more attenuation due to back reflection and absorbtion. On the other hand, reflective DMD surface consists of tightly builted micro-mirrors with $\sim$1μm gap that provides higher fill factor (ratio to pixel size of 10.8μm) of 90% than the LC-SLM with 70%.

3. The DMD can provide 6.6 times higher power transfer efficiency, that is the ratio of reflected irradiance to incident irradiance, than the LC-SLMs. As a result, DMD becomes more suitable for high power applications and same irradiance can be achieved with less exposure time.

4. The DMD performs $\sim$11 times and $\sim$3.3 times higher contrast ratio between maximum and minimum fluxes at the diffuser, for projected and holographic images, respectively.

5. The DMD generated images show slight artifacts mainly at the edges of micro-mirrors, however the LC-SLM generated images show much noticeable artifacts due to interference of multiple reflections from cascaded glass layers of the LCD.

6. The pixelated structure of both DMD and LC based spatial light modulators functions as a diffraction grating. The tilted surface due to states of micro-mirrors turns the DMD into a blazed diffraction grating with a blaze angle of θ_T (tilt angle). Thus, when illuminated at blaze angle (blaze condition $\alpha = \beta$) as twice as higher diffraction efficiency of 88% can be obtained than the LCD device.

7. DMD's mirrored surface can enable modulation of broadband light ranging from ultraviolent (UV) to near infra red (NIR). The DMD mirrors are also protected by a cover glass, which is coated to operate for desired spectral window [16].

Disadvantages :

1. The DMD can enable only amplitude modulation, since it only has a reflective mode. However, the LC-SLMs can be used both in reflective and transmissive modes that facilitate both amplitude and phase modulation.

2. The DMD mirror array as a 2D blazed diffraction grating with period of mirror pitch size (typically 10.8μm) distributes the incident beam into diffraction orders. The state of the micro-mirrors has no effect on the diffraction grating, only changes the corresponding power distribution over the diffraction orders. The diffractive nature of DMD causes degradation in the coupling efficiency and the higher diffraction orders create interference patterns, which appear as background noise, for especially broadband applications [16, 63].

4.3 Experimental Setup and System Description

Figure 4.4 illustrates the concept of novel 2D imaging system utilizing MEMS DMD technology. Ideally large area scanning is achieved by using N pulsed lasers with the same repetition rates. Each laser will send optical impulses to image different subsection of the imaging plane. Since detection system uses single photodetector, each pulse is generated with a constant delay, $n \times \tau, (n = 1, 2, 3, \ldots, N)$, where $N \times \tau \leq T$ =repetition rate. In the proposed system, N lasers array is replaced by a modelocked fiber laser as a master light source to generate broadband supercontinuum of light through nonlinear process [32]. Specifically, supercontinuum pulses are generated to provide broadband source by propagating the Mode Locked Laser pulses (at 1550nm with <1ps pulse width and 20MHz repetition rate) through a fiber-based system that consists of an EDFA and the cascaded single mode, dispersion shifted and nonlinear fiber patch cords. Band pass filter (CWDM) centered at 1590nm is used to carve out ~20nm nearly flat portion of the spectrum for scanning. In the first stage, carved SC pulses are wavelength-to-time mapped by using a dispersion compensation module with dispersion (D= -675ps/nm) for real time detection. In this step, group velocity dispersion is being used to create a time delay between different colors of the pulse and hence spread spectral content linearly in time domain. The timing requirement at this stage is imposed by the overlap between lasers after time stretching. The delay between consecutive pulses (τ) should be larger

than the chirped pulse width at the input of the circulator [2, 69, 70]. A pulse picking setup using optical switches follows the SC source and time wavelength mapping process to generate N parallel optical paths and to mimic the N independent lasers.

After time wavelength mapping, selected pulses are launched into free space by an array of collimators and followed by DMDs to facilitate 1D scanning. The optical pulses, on the other hand, are highly attenuated while passing through the system. The system losses are mainly due to the DCM (∼2.1dB insertion loss) and the DMD which induces single pass attenuation of ∼45% by considering the beam wavelength (1590nm), micro-mirror reflectivity (∼90%), active area (∼90%), diffraction efficiency (88%) and the protective cover glass on the micro mirrors (single pass transmission coefficient of ∼90% if coated for NIR and ∼75% if coated for visible) [48]. In the experimental setup, since power budget was not sufficient for simultaneous multichannel measurement, only one channel at a time has been used for scanning. Also, in order to compensate the system losses and to obtain a better signal to noise ratio, a flat gain Raman amplifier is designed to provide a uniform amplification through the DCM. The Raman amplification with ∼10dB net gain and <0.5dB gain ripple is introduced by using four pump diode lasers at wavelengths of 1450nm, 1470nm, 1490nm, and 1505nm in a hybrid pumping configuration.

In the second stage, the optical beam is expanded to illuminate the active area of the DMD, which consists of individually controllable micro mirror arrays. Here, we use DMD mirrors fabricated by Texas Instruments. By switching the state of individual micro mirrors from ON state to OFF state, the large optical beam is digitally divided into segments and mapped to different locations at the image plane and hence beam steering is achieved as shown in Fig. 4.5. The spectral content of the time stretched SC pulses is dispersed by the diffractive optics which is composed of a blazed diffraction grating and a Fourier lens to illuminate each location in space by different colors of light that arrive at different times. After being mapped over the focal plane, the spectrum of the pulses is modified by the reflection and transmission property of the target image. Through the time wavelength mapping process that was achieved in fibers, the spectral modulations are mapped to the time domain at the image plane. The spectrally and temporally modulated pulses via DMD are then captured by a photo detector (>1.2GHz bandwidth), which is placed at the optical path that corresponds mirrors' ON state direction, while at the OFF state, beams are blocked by the setup. A real time storage oscilloscope

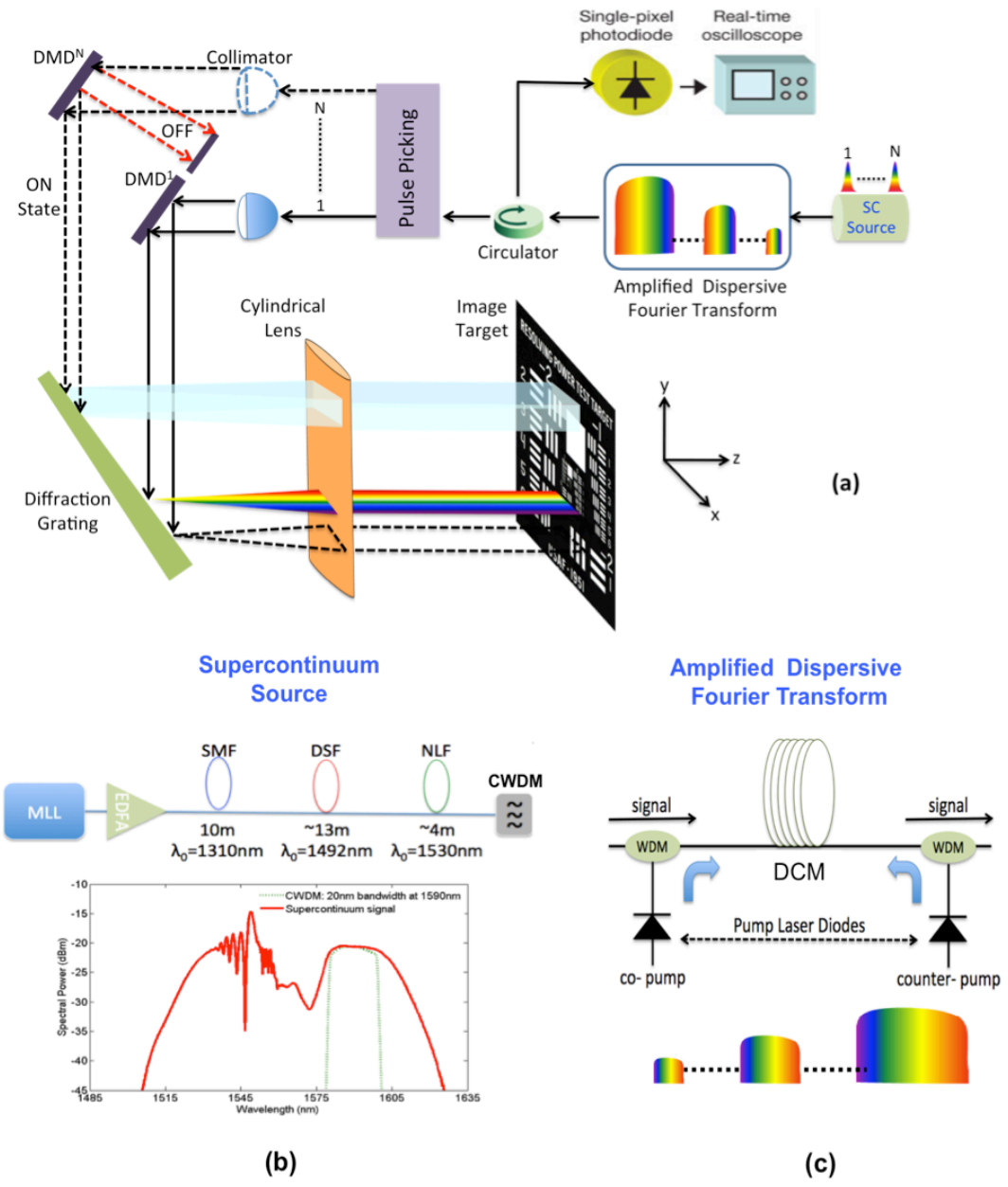

FIGURE 4.4: The experimental setup for all optical reflective parallelized N-channel dispersive laser scanner (a). The single channel setup is used for the proof-of-concept demonstration. The supercontinuum pulse generation (b) and the amplified dispersive Fourier transform (c) modules.

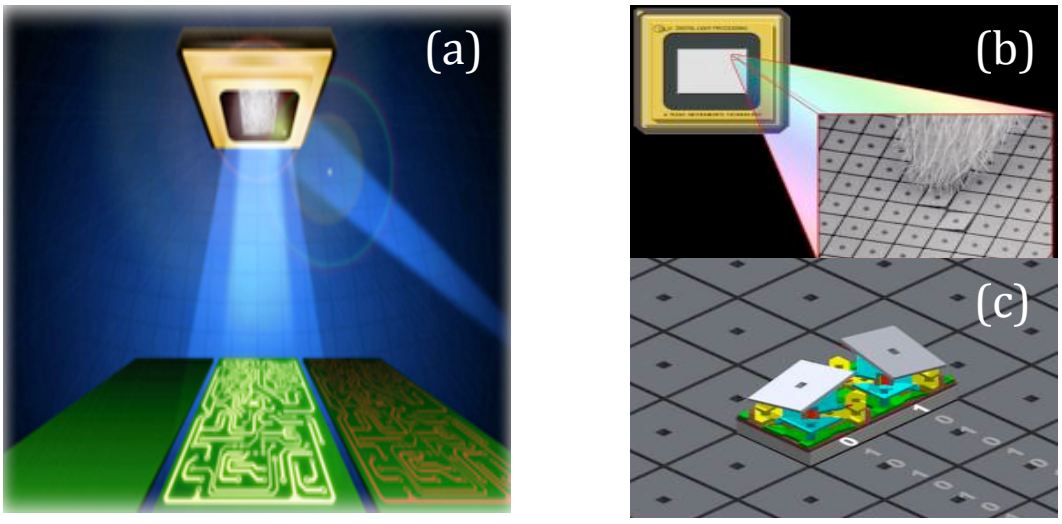

FIGURE 4.5: DMD as a programmable beam steering technology (a) [71]. A single DMD consisting 768x1024 micro mirrors and inset shows the SEM image of micro mirrors (b). Schematics of individual micro mirrors (c) [8].

with 8GHz RF bandwidth captures the electrical signals from the photodetector for post processing.

4.3.1 Lateral Scanning

The broadband optical pulses are spatially dispersed and focused over the space by using diffractive optics including diffraction gratings and Fourier lenses. Due to the pulse nature of the illumination, image modulation is captured by a single pulse and thus the lateral scanning rate is in megahertz, which is determined by laser repetition rate. The normalized intensity distribution $\bar{I}(x,\lambda)$, field of view (FOV) and the spatial (Δx) resolution of the pulse shaping system for both plane waves $E_p(x,d) \propto rect(x/d)$ and Gaussian waves $E_g(x,w) \propto exp(-0.5x^2/w^2)$ where $w = d/(2\sqrt{\ln 2})$ are calculated as [8]:

$$Gaussian : \bar{I}(x,\lambda) = \exp^2\left[-\frac{\pi^2(x-x_0)^2}{2\ln 2\lambda^2}\left(\frac{d}{f}\right)^2\right] \tag{4.1a}$$

$$Plane : \bar{I}(x,\lambda) = sinc^2\left[\frac{x-x_0}{\lambda}\left(\frac{d}{f}\right)\right] \tag{4.1b}$$

$$Gaussian : \Delta x \approx \frac{2\lambda f}{d\pi}\ln 2 \tag{4.1c}$$

$$Plane : \Delta x \approx \frac{2 \times 1.39156\lambda f}{d\pi} \tag{4.1d}$$

$$FOV \approx G_\beta f \Delta\lambda \tag{4.1e}$$

Here f is the lens focal length, d is the beam size, $x_0 \simeq G_\beta f(\lambda - \lambda_0)$ is the relative position of 1^{st} order diffraction peak with respect to central wavelength (λ_0) and G_β is the effective groove density, which is defined as a function of 1^{st} order diffraction angle, $G/\cos(\beta)$ [8]. The beam size is defined as the aperture size for plane waves, and full width at half maximum for Gaussian beams. The 1^{st} order diffraction angle (β) for the incident beam at wavelength (λ) and the incident angle (α) is calculated by using the grating equation as $\sin(\alpha) + \sin(\beta) = \lambda G$ which reduces to $2\sin(\beta) = \lambda G$ in a Littrow configuration ($\alpha = \beta$).

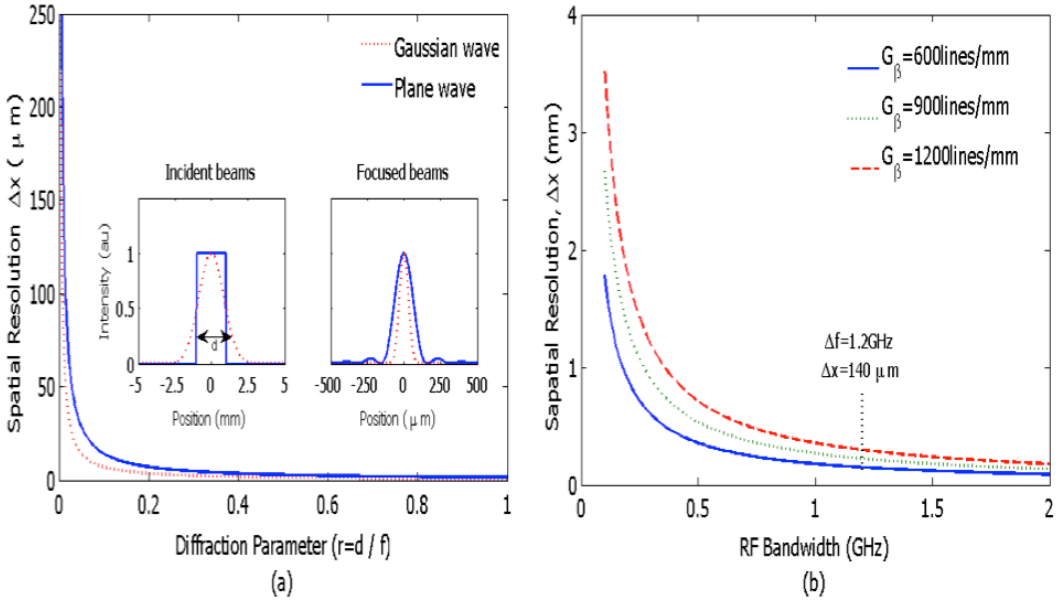

FIGURE 4.6: The spatial resolution of the focusing system depends on the diffraction limit and is impoved by increasing diffraction parameter, r=d/f (a). The temporal resolution (calculated for D= -675ps/nm) due to the RF bandwidth limits the spatial resolution via time-to-space mapping (b) [8].

Final resolution of the imaging system is defined not only by the diffraction limit but also by the temporal resolution (bandwidth) of the detection system. Figure 4.6 illustrates the achievable resolution with respect to key parameters of optical components and the RF detection system. According to Eq. (4.1d), the system resolution is optically limited by the diffraction limit ($r = d/f$) due to Fourier optics. By increasing the diffraction parameter ($r > 0.1$), the spatial resolution $< 10\mu m$ is achievable, as illustrated in Fig. 4.6a. In this proposed system, by changing the number of horizontal mirrors, DMD can enable tunability of the beam size and hence the diffraction limit. The lateral resolution of the system is mainly limited by the detection system. A photodetector with a given RF bandwidth (1.2GHz used in our experiments) limits the achievable temporal resolution ($\Delta t_{det} \approx 1/\Delta f$) to ~800ps which corresponds to spectral resolution ($\Delta\lambda_{det} \approx \frac{1}{\Delta f \cdot D}$) of

$\sim$1.2nm (due to uniform -675ps/nm dispersion) which translates into a spatial resolution of, $\Delta x_{det} \approx \frac{G_\beta f}{\Delta f \cdot D}) \approx 145\mu m$, via time-to-space mapping, as illustrated in Fig. 4.6b.

4.3.2 Vertical Scanning

In our proposed 2D imaging system, the vertical scanning is achieved by a DMD that is used as a beam steering device. At each vertical position, SC pulses directly capture the entire lateral image by using spatio-temporal dispersive imaging technique without scanning. The lateral resolution (Δx) is determined by 4-f imaging system, which consists of diffraction grating and a Fourier lens in a double pass system, and the resolution estimated by the width of the focused beam through Eq. (4.1d). Spatially and spectrally shaped pulses are then stretched over time by passing through the highly dispersive DCM for real time detection.

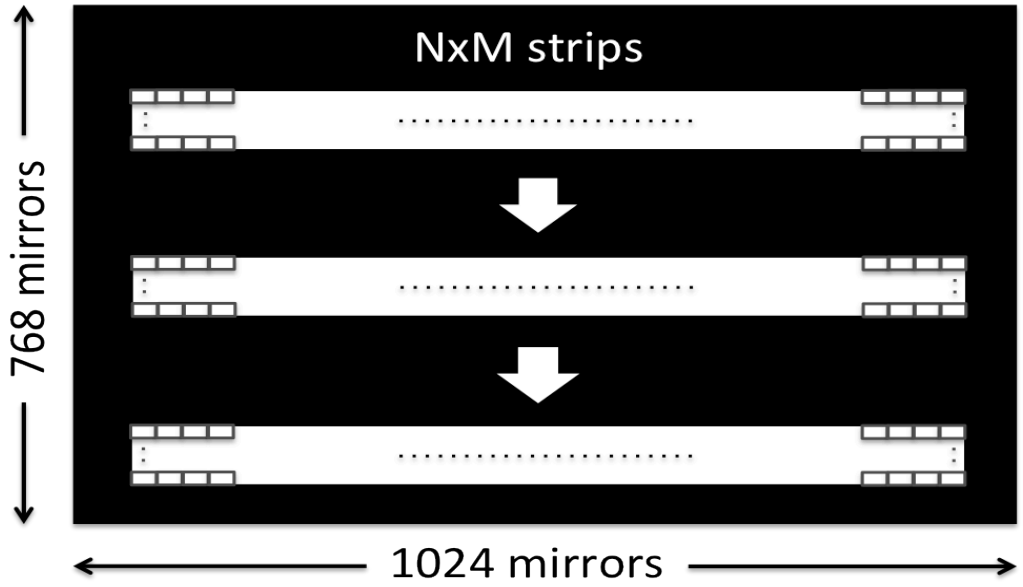

FIGURE 4.7: The horizontal strip-type binary patterns created on DMD for laser scanning. The position of the NXM spatial mask is vertically scanned over the object by loading DMD with these dynamic patterns.

Figure 4.7 illustrates the sample binary patterns created on DMD for beam steering. In these horizontal strip-type patterns, the white parts correspond to NxM arrays of ON state mirrors and the black parts correspond to OFF state mirrors. In the imaging experiment, first such horizontal strip patterns on DMD, namely narrow spatial masks, are created and then the light reflected by the mirror array is sent onto the object through a cylindrical lens. The vertical scanning is achieved by dynamically shifting this mask

at the DMD, which, as a result, shifts the reflected light onto the object. Consequently, the vertical (Δy) resolution is expected to be different from what is estimated by the Eq. (4.1c). Indeed, it is determined by the number of rows of mirror arrays that switch to the same state simultaneously or the size of masks on DMD surface. Hence, a use of N rows will create an optical beam where the vertical beam waist will be $N \times 10.8\mu m$, where 10.8μm is the mirror pixel size at the DMD chip. Increasing the number of rows in DMD array increases the SNR, since more optical power is reflected on to the object. However, it will decrease the vertical resolution, since the width of the reflected light on image increased. The vertical scanning speed is the second crucial parameter in the proposed experimental system and it is determined by the frame rate of DMD. Experimentally, DMDs with 32.5kHz scanning speed (~30μs switching time) can achieve ~600 laser pulses to illuminate the same subsection or 600 subsections for pulse picking at the same laser pulse rate (20MHz / 32.5kHz).

4.4 Experimental Results

Real time imaging can work in reflection or transmission mode. To demonstrate 2D fast scanning capability, we used the time-space-wavelength mapping technique working in the reflection mode. The target image scanned by the DMD is recorded by the series of SC pulses. This 1D pulse stream (stream of horizontal line scans) with 50ns time aperture is then segmented for different vertical coordinates, vertically aligned and digitally processed to extract the spatial features and reconstruct the original 2D image.

In this experimental study, we have used optical beam with ~5mm beam size, diffraction grating with 600lines/mm, lens with 200mm focal length, DMD (0.55-inch diagonal mirror arrays, 1024x768 individually addressable aluminum micro mirrors, 10.8μm pitch size, discrete states of ON (+12^o rotation) or OFF (-12^o rotation), and frame rate of 5kHz) and 15×600 horizontal excitation strips to vertically scan the target image (USAF test chart) which consists of vertical black and white strips with different spatial frequencies. The proposed system can scan ~20mm^2 wide area [~3mm lateral ($FOV_{lateral} = G_\beta f \Delta\lambda$) and ~7.6mm vertical ($FOV_{vertical} = 768 \times 10.8\mu m$) with 20MHz (pulse repetition rate) in 1D and 5kHz (DMD frame rate) in 2D.

Figure 4.8 illustrates the lateral resolution performance of the dispersive imaging system. The 2D image of five groups of vertical bars with dimensions varying from ~150μm to ~220μm is captured by our dispersive laser scanner. The temporal modulation (due to spatial/spectral pulse shaping) of the SC pulses by the vertical bars with varying spatial frequencies is shown in Fig. 4.8. Due to the diffraction limit of the focusing system, as the spatial frequency of the patterns increases, the modulation depth decreases. Thus, we used vertically wider excitation strips (N=15 mirrors) to increase the signal to noise ratio at the expense of diminishing vertical resolution to ~160μm compared to 10.8μm vertical resolution that is achievable by using narrow strips of N=1. In addition, vertically wider strips shifted by certain number (n<N) of pixels (overlapping strips) can be used to increase the SNR and to achieve higher vertical resolution (n × 10.8μm).

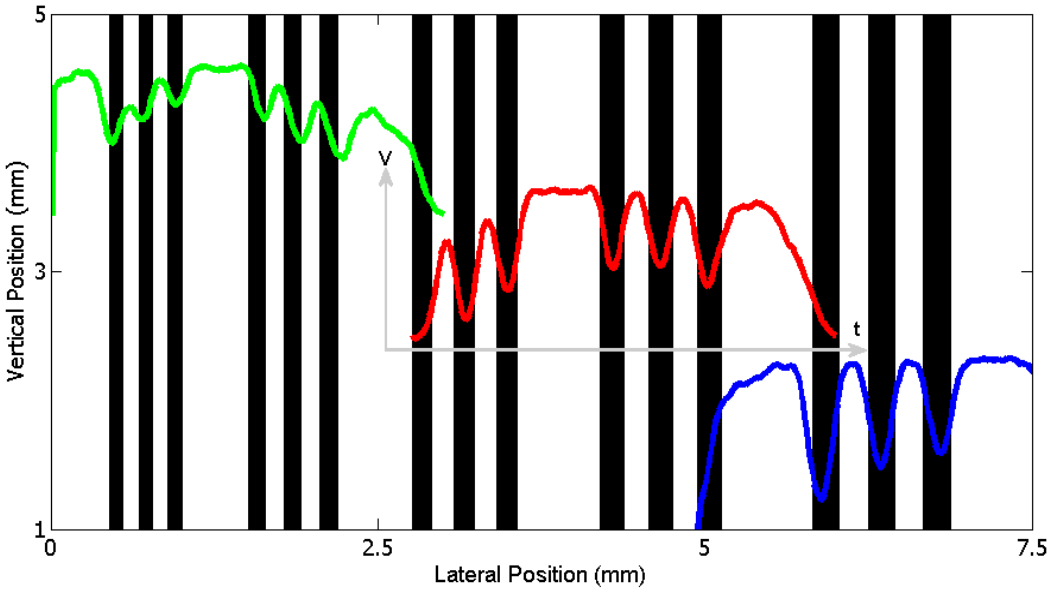

FIGURE 4.8: The lateral resolution performance of space wavelength mapping. The vertical bars with dimensions of ~150μm to ~220μm are captured by the ~13.5ns SC pulses.

Figure 4.9 compares the 2D CCD image and the reconstructed images of the test target (Fig. 4.9a: USAF test chart) captured by our MEMS based dispersive laser scanner. The image is reconstructed by mapping the reflection from the target encoded on the pulse train at different scanning positions into a 2D matrix. Dynamically shifting the 15×600 excitation strips over the DMD at 5kHz rate, the target is scanned with a resolution of ~150μm (lateral) and ~160μm (vertical). The captured image clearly shows the vertical and horizontal bars: Group=1, Element 3-6 (Fig. 4.9b) and Group=0, Element 5-6 (Fig. 4.9c).

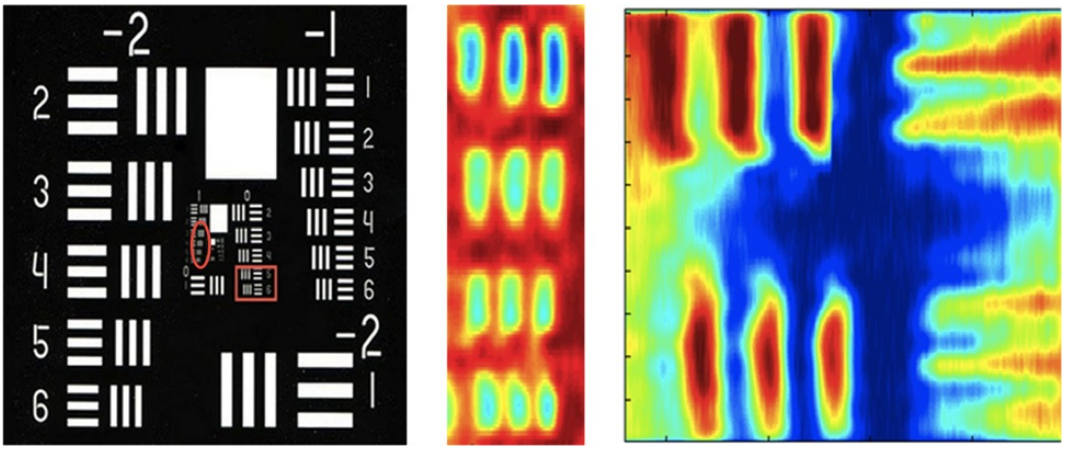

FIGURE 4.9: Comparison between a CCD image (a) and a digitally reconstructed scan image of the target: USAF test chart Group=1, Element 3-6 [width / line 198μm-140μm] (b) and Group=0, Element 5-6 [width / line 314μm-280μm] (c).

To construct the image the normalized intensity distribution $\bar{I}(x,\lambda)$ calculated in Eq. (4.1a) is nearly same for all the wavelengths within 20nm spectral window centered at 1590nm (λ_0). Thus, the intensity distribution for each wavelength is approximated as:

$$\bar{I}_0(x) \simeq \bar{I}(x,\lambda_0) \tag{4.2a}$$

$$I(x,\lambda) \simeq F(\lambda)\cdot\bar{I}_0(x-x_0) \tag{4.2b}$$

where $I(x,\lambda)$ is the intensity distribution and $F(\lambda)$ is the spectral power density. The space-to-wavelength mapped optical beam is both spatially and spectrally shaped by the target image m(x), which can be modeled as a convolution at Fourier plane.

$$y(\lambda) \simeq F(\lambda)\cdot\int_{-\infty}^{\infty}\bar{I}_0(x-x_0)\cdot m(x)dx = F(\lambda)\cdot conv[I(x,\lambda),m(x)] \tag{4.3}$$

Spectrally encoded signals are converted into time domain $\left[y(\lambda)\xrightarrow[mapping]{frequency-to-time} y(t)\right]$ via dispersive Fourier transformation through highly dispersive fibers. By neglecting the higher order dispersion terms, namely assuming a uniform dispersion over a wide spectrum, the temporal mapping is modeled linear as $\Delta t = D\cdot\Delta\lambda$ where Δt is the temporal position of the wavelengths relative to the reference wavelength. By using such digital signal processing techniques as digital filtering and deconvolution, the spatial information of the target, m(x), can be extracted.

The system performance of current experimental approach of this real time imaging, however, is limited in terms of the spatial resolution, field of view and the power efficiency due to following reasons. The diffraction prevents the use of bulk Fourier lenses with long focal lengths ($\propto \lambda f/d$) and hence limits the spatial resolution. Also, 1cm^2 active area of the DMD combined with diffraction gratings ($\sim$3.5^o/100nm spatial dispersion with 600lines/mm groove density) limits the field of view. Finally, high losses due to higher order diffractions limit the power efficiency of the system. In order to achieve resolution close to 20μm and lower, the system should be able to illuminate the whole imaging sample with frequency-time and space-time mapped light, focus the light everywhere on the sample to $<$20μm spot size and should be low loss for high contrast imaging. Furthermore, in order to make the system compatible with manufacturing technology the working distance should be long, $>$0.5mm to avoid contact and contamination. Planar optical devices such as lenses or diffraction optics combined with real time imaging can facilitate high resolution imaging in real time.

4.5 Conclusion

We have proposed a fast dispersive laser scanning system by using MEMS micro mirror technology. Two-dimensional beam steering is employed by combining the space wavelength mapping for the lateral scanning and digital micro mirror arrays for vertical scanning. By dynamically switching the states of the micro mirrors, the position of the spatially dispersed beam is moved over the target. We have monitored $\sim$20mm^2 wide area with $\sim$150μm lateral and $\sim$160μm vertical resolution for the proof of concept. We estimate that MEMS based amplified time stretched system can achieve fast vertical scanning with frame rates up to 32.5kHz and with resolution down to single mirror pitch size of 10.8μm.

Bibliography

[1] W. Caputi. Stretch: A time-transformation technique. *IEEE Transactions on Aerospace and Electronic Systems*, AES-7(2):269–278, March 1971.

[2] S. K. Kalyoncu, Y. Huang, Q. Song, and O. Boyraz. Analytical study on arbitrary waveform generation by MEMS micro mirror arrays. *Optics Express*, 20(25):27542–27553, 2012.

[3] J. Azana, L. R. Chen, M. A. Muriel, and P. W. E. Smith. Experimental demonstration of real-time Fourier transformation using linearly chirped fiber bragg gratings. *Electronic Letters*, 35:2223–2224, 1999.

[4] K. Goda, A. Mahjoubfar, C. Wang, A. Fard, J. Adam, D. R. Gossett, A. Ayazi, E. Sollier, O. Malik, E. Chen, et al. Hybrid dispersion laser scanner. *Scientific reports*, 2, 2012.

[5] F. Coppinger, A. S. Bhushan, and B. Jalali. Time magnification of electrical signals using chirped optical pulses. *Electronic Letters*, 34(4):399–400, February 1998.

[6] A. S. Bhushan, F. Coppinger, and B. Jalali. Time stretched analogue-to-digital conversion. *Electronic Letters*, 34(9):839–840, April 1998.

[7] F. Coppinger, A. S. Bhushan, and B. Jalali. Photonic time stretch and its application to analog-to-digital conversion. *IEEE Transactions on Microwave Theory and Techniques*, 47(7):1309–1314, 1999.

[8] S. K. Kalyoncu, R. Torun, Y. Huang, Q. Zhao, and O. Boyraz. Fast dispersive laser scanner by using digital micro mirror arrays. *ASME Journal of Micro- and Nano-Manufacturing*, 2:021004–1–021004–6, June 2014.

[9] K. Goda, K. Tsia, and B. Jalali. An ultrafast barcode reader using amplified dispersive Fourier transform. pages 644–645. IEEE Lasers and Electro-Optics Society 2008, 9-13 November 2008 2008.

[10] S. P. Singh and N. Singh. Nonlinear effects in optical fibers: Origin, management and applications. *Progress In Electromagnetics Research*, 73:249–275, 2007.

[11] G. P. Agrawal. *Nonlinear Fiber Optics*. Academic Press, US, 3 edition, 2009.

[12] O. Boyraz. 285A lecture slides 3, 2014. URL `https://eee.uci.edu/14w/18710/Notes3_Temp.pdf`. [Online; accessed 10-June-2014].

[13] G. P. Agrawal. *Fiber-Optic Communication Systems*. John Wiley & Sons, 3 edition, 2002.

[14] M. N. Islam, L. F. Mollenauer, and R. H. Stolen. Cross-phase modulation in optical fibers. *Optics Letters*, 12(8), 1987.

[15] B. Washburn. Numerical solutions to nonlinear schrodinger equation. URL `http://www.phys.ksu.edu/personal/washburn/pdf/washburn_thesis_chapter4.pdf`. [Online; accessed 10-June-2014].

[16] S. K. Kalyoncu. *Raman Based Dispersive Systems for Short Pulse Generation and Optical Signal Processing*. PhD thesis, University of California, Irvine, 2013.

[17] A. Hasegawa and Y. Kodama. *Solitons in optical communications*. Clarendon Press Oxford, 1995.

[18] A. Hasegawa and Y. Kodama. Amplification and reshaping of optical solitons in a glass fiber-I. *Optics letters*, 7(6):285–287, 1982.

[19] M. Nakazawa, K. Suzuki, and Y. Kimura. 3.2-5 Gb/s, 100km error free soliton transmissions with erbium amplifiers and repeaters. *IEEE Photonic Technology Letters*, 2(3):216–219, 1990.

[20] H. Rong, S. Xu, O. Cohen, O. Raday, M. Lee, V. Sih, and M. Paniccia. A cascaded silicon Raman laser. *Nature photonics*, 2(3):170–174, 2008.

[21] R. H. Stolen. Fundamentals of raman amplification in fibers. In M. N. Islam, editor, *Raman amplifiers for telecommunications*, volume 1, chapter 2. Springer, 2004.

[22] C. V. Raman. A new radiation. *Indian Journal of physics*, 2:387–398, 1928.

[23] H. A. Haus and M. Nakazawa. Theory of the fiber raman soliton laser. *JOSA B*, 4 (5):652–660, 1987.

[24] J. Bromage. Raman amplification for fiber communications systems. *Journal of Lightwave Technology*, 22(1):79, 2004.

[25] RP Photonics Encyclopedia. Erbium-doped gain media. URL `http://www.rp-photonics.com/erbium_doped_gain_media.html`. [Online; accessed 10-June-2014].

[26] J. Chou, O. Boyraz, D. Solli, and B. Jalali. Femtosecond real-time single-shot digitizer. *Applied Physics Letters*, 91(16):161105–161105, 2007.

[27] S. K. Kalyoncu, Y. Huang, E. K. Tien, E. Adas, D. Yildirim, and O. Boyraz. Noise performance of time stretch system with distributed and discrete amplifiers. In *CLEO: Science and Innovations*, page CTuA7. Optical Society of America, 2011.

[28] B. Jalali, K. Goda, A. Fard, and S. H. Kim. From analog to digital conversion to blood screening; evolution of photonic time stretch. In *CLEO: Science and Innovations*, page CWC3. Optical Society of America, 2011.

[29] Y. Han and B. Jalali. Photonic time-stretched analog-to-digital converter: Fundamental concepts and practical considerations. *Journal of Lightwave Technology*, 21 (12):3085, 2003.

[30] P. V. Kelkar, F. Coppinger, A. S. Bhushan, and B. Jalali. Time-domain optical sensing. *Electronics Letters*, 35(19):1661–1662, 1999.

[31] K. Goda, K. Tsia, and B. Jalali. Serial time-encoded amplified imaging for real-time observation of fast dynamic phenomena. *Nature*, 458(7242):1145–1149, 2009.

[32] O. Boyraz, J. Kim, M. N. Islam, E. Coppinger, and B. Jalali. 10 Gb/s multiple wavelength, coherent short pulse source based on spectral carving of supercontinuum generated in fibers. *Lightwave Technology, Journal of*, 18(12):2167–2175, 2000.

[33] S. Dubovitsky, W. H. Steier, S. Yegnanarayanan, and B. Jalali. Analysis and improvement of Mach-Zehnder modulator linearity performance for chirped and tunable optical carriers. *Journal of lightwave technology*, 20(5):858, 2002.

[34] Y. H. Kuo, W. H. Steier, S. Dubovitsky, B. Jalali, et al. Demonstration of wavelength-insensitive biasing using an electrooptic polymer modulator. *IEEE Photonics Technology Letters*, 15(6):813–815, 2003.

[35] Tech-Etch. Photoetched fuel cell plates, frames, support screens & end caps. URL `http://www.tech-etch.com/photoetch/fuelcell.html`. [Online; accessed 10-June-2014].

[36] International Partnership for Hydrogen and Fuel Cells in the Economy. The role of battery electric vehicles, plug-in hybrids and fuel cell electric vehicles. URL `http://www.iphe.net/docs/Resources/Power_trains_for_Europe.pdf`. [Online; accessed 10-June-2014].

[37] G. Wilkening and H. Bosse. Nano- and micrometrology state-of-the-art and future challenges. *MAPAN-Journal of Metrology Society of India*, 20(2):125–151, 2005.

[38] H. N. Hansen, G. Tosello, S. Gasparin, and L. De Chiffre. Dimensional metrology for process and part quality control in micro manufacturing. *International Journal of Precision Technology*, 2(2):118–135, 2011.

[39] H. U. Danzebrink, L. Koenders, G. Wilkening, A. Yacoot, and H. Kunzmann. Advances in scanning force microscopy for dimensional metrology. *CIRP Annals-Manufacturing Technology*, 55(2):841–878, 2006.

[40] J. C. Wyant. White light extended source shearing interferometer. *Applied Optics*, 13(1):200–202, 1974.

[41] M. Minsky. Memoir on inventing the confocal scanning microscope. *Scanning*, 10 (4):128–138, 1988.

[42] G. F. Marshall and G. E. Stutz. *Handbook of optical and laser scanning*. CRC Press, 2004.

[43] T. Fujii and T. Fukuchi. *Laser remote sensing*. CRC Press, 2005.

[44] C. Dotson, R. Harlow, and R. L. Thompson. *Fundamentals of dimensional metrology*. Thomson Learning, 2003.

[45] C. Weitkamp. *Range-resolved optical remote sensing of the Atmosphere*. Springer, 2005.

[46] B. Schwarz. Mapping the world in 3d. *Nat. Photonics*, 4(7):429–430, 2010.

[47] A. Sinha. *Vibration of mechanical systems*. Cambridge University Press, 2010.

[48] W. Osten. *Optical inspection of microsystems*. CRC Press, 2006.

[49] J. A. Pelesko and D. H. Bernstein. *Modeling Mems and Nems*. CRC press, 2002.

[50] G. Popescu, T. Ikeda, K. Goda, C. A. Best-Popescu, M. Laposata, S. Manley, R. R. Dasari, K. Badizadegan, and M. S. Feld. Optical measurement of cell membrane tension. *Physical review letters*, 97(21):218101, 2006.

[51] W. Göbel, B. M. Kampa, and F. Helmchen. Imaging cellular network dynamics in three dimensions using fast 3d laser scanning. *Nature methods*, 4(1):73–79, 2006.

[52] J. B. Pawley. Handbook of biological confocal microscopy. 1995.

[53] W. Denk, J. H. Strickler, W. W. Webb, et al. Two-photon laser scanning fluorescence microscopy. *Science*, 248(4951):73–76, 1990.

[54] A. Hoffman, M. Goetz, M. Vieth, P. R. Galle, M. F. Neurath, and R. Kiesslich. Confocal laser endomicroscopy: technical status and current indications. *Endoscopy*, 38(12):1275–1283, 2006.

[55] A. Tárnok and A. O. H. Gerstner. Clinical applications of laser scanning cytometry. *Cytometry*, 50(3):133–143, 2002.

[56] R. Conant. *Micromachined mirrors*, volume 12. Springer, 2002.

[57] Z. Yaqoob and N. A. Riza. Passive optics no-moving-parts barcode scanners. *Photonics Technology Letters, IEEE*, 16(3):954–956, 2004.

[58] D. R. Pape, A. P. Goutzoulis, and S. V. Kulakov. *Design and fabrication of acousto-optic devices*. M. Dekker, 1994.

[59] I. W. Jung, J. Wang, and O. Solgaard. Optical pattern generation using a spatial light modulator for maskless lithography. *Selected Topics in Quantum Electronics, IEEE Journal of*, 13(2):147–154, 2007.

[60] D. Dudley, W. M. Duncan, and J. Slaughter. Emerging digital micromirror device (dmd) applications. In *Micromachining and Microfabrication*, pages 14–25. International Society for Optics and Photonics, 2003.

[61] S. K. Nayar, V. Branzoi, and T. E. Boult. Programmable imaging using a digital micromirror array. In *Computer Vision and Pattern Recognition, 2004. CVPR 2004. Proceedings of the 2004 IEEE Computer Society Conference on*, volume 1, pages I–436. IEEE, 2004.

[62] DLP Texas Instruments. Dlp 0.55xga chipset, 2010. URL `http://www.ti.com/lit/ml/dlpb003/dlpb003.pdf`. [Online; accessed 10-May-2013].

[63] R. S. Nesbitt, S. L. Smith, R. A. Molnar, and S. A. Benton. Holographic recording using a digital micromirror device. In *Electronic Imaging'99*, pages 12–20. International Society for Optics and Photonics, 1999.

[64] L. J. Hornbeck et al. Digital light processing for high-brightness, high-resolution applications. In *Proc. SPIE*, volume 3013, pages 27–40, 1997.

[65] DLP Texas Instruments. Mems dlp technology - getting started, 2010. URL `http://www.ti.com/dlp`. [Online; accessed 10-May-2013].

[66] DLP Texas Instruments. Application report: Dmd 101: Introduction to digital micromirror device (dmd) technology, 2008. URL `http://www.ti.com/lit/an/dlpa008/dlpa008.pdf`. [Online; accessed 10-May-2013].

[67] DLP Texas Instruments. Application report: Dlp system optics, 2010. URL `http://www.ti.com/lit/an/dlpa022/dlpa022.pdf`. [Online; accessed 10-May-2013].

[68] DLP Texas Instruments and ASME. The digital micromirror device: A historic mechanical engineering landmark, 2008. URL `http://files.asme.org/asmeorg/Communities/History/Landmarks/14607.pdf`. [Online; accessed 10-May-2013].

[69] S. K. Kalyoncu, Y. Huang, Q. Song, and O. Boyraz. Fast arbitrary waveform generation by using digital micromirror arrays. *Photonics Journal, IEEE*, 5(1): 5500207–5500207, 2013.

[70] S. K. Kalyoncu, Y. Huang, R. Torun, Q. Zhao, and O. Boyraz. Fast dispersive laser scanner by using digital micro mirror arrays. In *CLEO: Applications and Technology*, pages JTu4A–30. Optical Society of America, 2013.

[71] DLP Texas Instruments. Digital exposure, 2010. URL `http://www.ti.com/analog/docs/memsmidlevel.tsp?sectionId=622&tabId=2455`. [Online; accessed 10-May-2013].